

Highlights

Machine Learning for the Characterisation of Sustainable Supercapacitors from Electrochemical Molten-Salt Tire-Derived Carbon

Maria A. Sandoval-Riofrio, Kavisha Jayathunge

-
-
-

Machine Learning for the Characterisation of Sustainable Supercapacitors from Electrochemical Molten-Salt Tire-Derived Carbon

Maria A. Sandoval-Riofrio^{a,*1}, Kavisha Jayathunge^{a,2}

^aBournemouth University, Talbot Campus, Fern Barrow, Poole BH12 5BB, Dorset, UK

ARTICLE INFO

Keywords:

Supercapacitors
Machine learning
Electrochemical molten salts
Black carbon

ABSTRACT

This study explores the development of sustainable supercapacitors using electrochemically activated carbon derived from plastic and tyre waste as electrode materials and ethaline, a deep eutectic solvent, as a green electrolyte. The electrochemical molten salts (EMS) process was employed to activate black carbon, a waste byproduct from tyre recycling, resulting in significant enhancements in carbon properties, including a 39.4% increase in BET surface area (from $43.10 \text{ m}^2 \cdot \text{g}^{-1}$ to $60.09 \text{ m}^2 \cdot \text{g}^{-1}$) and improved pore volume and size distribution. These findings establish the EMS process as a scalable and effective method for producing high-performance porous carbon materials.

Supercapacitors assembled with EMS-activated carbon and ethaline exhibited remarkable electrochemical performance, achieving a specific capacitance by GCD of $92.2 \text{ F} \cdot \text{g}^{-1}$ at $0.4 \text{ A} \cdot \text{g}^{-1}$, and $110.16 \text{ F} \cdot \text{g}^{-1}$ by cyclic voltammetry, surpassing many conventional aqueous and organic systems. Combined CV and EIS analyses revealed primarily capacitive behaviour with notable contributions from diffusion processes in the activated carbon by EMS. Multiple machine learning model configurations for predicting specific capacitance showed that incorporating an area-based loss consistently improves accuracy and stability across runs. The best-performing model achieves an average error of 3.75%, compared with a baseline error of 15.49%. Analysis of the model's learned weights indicates that electrolyte temperature in the EMS process is the dominant factor influencing BC6 energy storage performance measured by specific capacitance, followed closely by active mass and electrolysis voltage.

These results highlight the potential of integrating waste-derived carbon materials with environmentally friendly electrolytes to create efficient, sustainable energy storage systems, while machine-learning-based performance assessment supports reproducibility and reduces experimental redundancy, minimising material, and energy waste during manufacturing.

1. Introduction

In an era where environmental sustainability is of primary importance for anthropogenic activities at all scales, it is crucial to find innovative solutions to reduce energy consumption and minimise carbon footprint. Capacitors are energy storage components that play a vital role in various systems but also offer important environmental benefits and technical advantages compared to other energy storage devices like batteries [7, 39, 1]. In recent years, more efficient supercapacitors (SCs) have been developed and are leading the market as they are fulfilling the gaps in the applications where batteries present limitations including thermal stability, extended long life, and maintenance-free operation [7, 39, 74]. Electrochemical energy storage devices, such as batteries or electrochemical capacitors, store energy by converting electrical energy into chemical energy, and active materials influence the cycling stability and lifespan of the device [71]. Porous materials for SCs play a key role in the energy storage performance. An electric double-layer capacitor

(EDLC) offers higher capacitance and energy density than an electrolytic capacitor. The efficiency of a supercapacitor is influenced mainly by the selection of electrode material. One of the most remarkable characteristics of a high-performance capacitor is possessing a large surface area electrode material that also has considerable compatibility with the selected electrolyte [39, 74]. Current SC electrodes employ carbon-based materials as active materials with diverse surface areas, for instance, activated carbon (AC) possesses a surface area between ~ 575 and $3000 \text{ m}^2 \cdot \text{g}^{-1}$ [36, 50, 28], functionalised carbon nanotubes (CNTs) in ranges of ~ 50 and $1315 \text{ m}^2 \cdot \text{g}^{-1}$ [72, 16, 62] and the most popular for energy storage purposes due to their exceptional conductivity properties is graphene (surface area of $\sim 2630 \text{ m}^2 \cdot \text{g}^{-1}$) [21, 64]. Charcoal, conducting polymers, and metal oxides have been also employed as electrode materials, nonetheless, the synthesis methods and the combination of them with carbon-based materials require innovative techniques that allow the production of efficient SCs utilising active materials sourced from alternative origins or waste streams [4]. By integrating these sustainable materials, energy storage technologies can become more competitive, adaptable to specific market needs, and scalable for large-scale applications [88].

Conversely, the high demand for advanced electrode materials requires new technology and feedstocks which is attracting particular attention due to the drawbacks of the mining of raw materials and environmental limitations of existing technologies to synthesise cathode active materials (CAM) along with composites with enhanced electrochemical

*Corresponding author

 msandoval2@bournemouth.ac.uk (M.A. Sandoval-Riofrio);
kjayathunge@bournemouth.ac.uk (K. Jayathunge)

 <https://www.linkedin.com/in/maria-a-sandoval/> (M.A. Sandoval-Riofrio);
<https://staffprofiles.bournemouth.ac.uk/display/kjayathunge> (K. Jayathunge)

ORCID(s): 0000-0003-0680-4539 (M.A. Sandoval-Riofrio);
0009-0006-5162-5731 (K. Jayathunge)

¹School of Computing and Engineering

²National Centre for Computer Animation

capacitance [7, 74]. The synthesis and activation of carbon-based porous materials have attracted considerable interest due to their potential as highly effective electrode materials in supercapacitor design. They possess outstanding mechanical strength, large specific surface area, and, most importantly, superior electrical conductivity [33, 66, 97]. Nevertheless, traditional methods for producing electrodes are often complex and resource-demanding, frequently involving scarce and hazardous substances [97].

This leads to additional expenditure and escalates in costs but also results in significant environmental consequences. Additionally, the current methods of carbon activation and the augmentation of specific surface area like pyrolysis, have been utilised in the last decades [42]. Pyrolysis involves using an inert environment to shield organic materials from oxidation and requires high temperatures to modify the morphology and physiochemical properties of carbon. In terms of sustainability, it is remarkable to introduce less energy-consuming technologies and feedstock circularity concepts within advanced materials manufacturing [100]. Within this context, plastic waste seems a feasible carbon source especially if it represents a major global plastic pollutant like tyre waste. Around 24 million tyres are sold every year, and their disposal leads to a significant environmental impact [87, 95]. Tyres possess a complex mix of materials including reinforced rubber and additives, making recycling challenging, particularly when converting tyre carbon into commercial products like black carbon that must meet standards for market competitiveness, commercial viability and scalability [22, 81, 87].

Conversely, these conventional approaches are being increasingly challenged by new methodologies that prioritise process integration, resource efficiency, and reduced environmental impact. In this study, electrochemical molten salts are discussed as an alternative to increasing the surface area and nanoporous of tyre pyrolysed carbon [97, 100, 37]. Electrochemical molten salts (EMS) technology has gained significant importance in recent years due to its versatility with various salts, temperatures, and voltages. On the other hand, EMS is widely applied for materials processing such as steel, non-ferrous and rare earth metal industries for refining and precision heat treatment processes limited by thermodynamic or kinetic factors [63]. In the last years, renewable energy infrastructure, lithium batteries, supercapacitors, hydrogen fuel cells, semiconductors, and other pioneering green and carbon-reduced technologies have been linked to developing new metal materials. EMS has become a popular technology due to its potential to recover critical metals, hydrogen obtention, and CO₂ capture by electrolysis [40, 60, 106]. Carbon sources like carbon black (a virgin feedstock commonly) is often misused and confused with black carbon (BC). Carbon black (CB) represents raw materials commercialised at a large scale and is part of other value and supply chains. On the other hand, Black carbon (BC) is not produced at a large scale to be commercialised and the coined term BC refers to fine particles normally sourced as an unwanted byproduct/residues of other manufacturing

processes such as pyrolysis or other manufactured products including fossil fuels (char, tar, coal-tar), plastic, rubber amongst others [61]. Under this framework, a novel method to convert pyrolysed plastic from tyre waste (BC) is proposed as an activation method to promote nanoporous formation by the electrochemical molten salt process. Adopting a sustainable technology approach, the electrochemical performance of the obtained nanoporous carbon was tested as cathode-anode active materials and their interaction with green electrolytes was evaluated in supercapacitors.

To accelerate the transition of laboratory-scale research into scalable manufacturing of supercapacitors, it is essential to optimise processing conditions and understand their impact on device performance. In this work, machine learning (ML) tools are employed as a data-driven approach to bridge the gap between laboratory-scale R&D and series production. Specifically, ML is used to investigate the influence of EMS processing parameters on the electrochemical energy storage behaviour of the resulting materials. The analysis focuses on correlating process conditions with specific capacitance, enabling predictive optimization of material performance and supporting scalable manufacturing strategies. Electrochemical systems are inherently multi parameter and nonlinear, with electrode microstructure, electrolyte composition, and EMS activation conditions interacting in ways that are difficult to disentangle through conventional parametric studies alone [47, 77]. ML is increasingly used in electrochemical energy-storage research for performance assessment, sensitivity analysis, and reduction of experimental redundancy, enabling researchers to map complex input-output relationships and identify the most influential variables without exhaustive trial-and-error experimentation at scaling-up stage [77, 30, 70]. In this study, ML models are trained on experimentally obtained EMS-activated carbon data to correlate material activation process signifiers (e.g., temperature, retention time and voltage), with key electrochemical metrics performed in a symmetric two-electrode supercapacitor configuration. Since both electrodes are identical and contribute equally to charge storage, the specific capacitance was calculated by normalizing the capacitance to the active mass of a single electrode (half-cell basis) [39, 86, 25]. Accordingly, the mass used in the ML analysis corresponds to half of the total active mass of the device, thereby supporting mechanistic interpretation while remaining grounded in empirical measurements.

ML can also contribute to faster scale-up and manufacturing of EMS-activated carbons by guiding the design of efficient experimentation and repeatability experiments on SCs manufacturing [11, 111]. Recent studies demonstrate that ML-assisted optimisation of synthesis and operating parameters can significantly reduce the number of required experiments while improving target electrochemical performance, which accelerates the transition from lab-scale to pilot- and industrial-scale production [67, 55, 90, 80, 83]. By combining ML based performance prediction with sensitivity analysis, R&D on SCs can prioritise robust, high yield regions of parameter space, minimise costly over testing, reduce

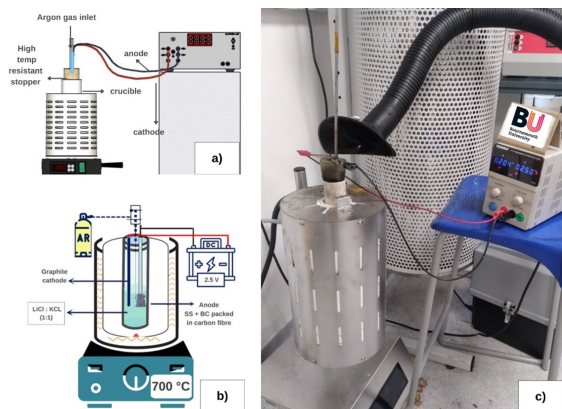


Figure 1: a) Computer-aided scheme of EMS reactor. b) Best parameters for black carbon activation and c) EMS reactor set-up.

the waste generated at laboratory scale and support “smart manufacturing” strategies for electrochemical materials. In this work, ML is limited to performance characterisation and post synthesis analysis of the tire wasted-derived carbon and is not used for real time control of the EMS activation process.

2. Experimental section

2.1. Electrochemical activation of black carbon

The EMS procedure was conducted within a sealed electrochemical cell (Nabertherm Tube Furnace RT 50) utilising a mixture of 50 g of LiCl and 50 g of KCl salts as electrolytes (Sigma Aldrich, 99%) in a 1:1 molar ratio. The molten salts to form the eutectic mixture, molar ratio and operation parameters were determined based on prior experimentation and based on literature [86, 52, 109]. Optimal operational conditions were identified under an Ar atmosphere as follows: 2 hours, a constant current of 0.2 A at 2.5 V, and a temperature of 700 °C, as illustrated in Figure 1. For electrochemical conversion, the cathode employed was a graphite rod of 1 mm diameter (graphite, 99.95%). The anode comprised a stainless-steel rod with approximately 0.3% nickel content combined with a black carbon (BC) sample that was pre-packed into carbon fibre in a cylindrical shape. The activated BC (BC6) was characterised after EMS activation and used to assemble SC electrodes.

2.2. Fabrication of activated carbon electrodes for the SCs

Electrodes were prepared by mixing the BC and activated carbon post-EMS BC6 as carbon active material (95% w/w) with 5% w/w polyvinylidene fluoride (PVDF) binder (Sigma-Aldrich, 10% suspension in N-methyl-pyrrolidone, NMP) in a slurry with NMP. The slurry was stirred for 6 hours at 3000 rpm and subsequently coated on aluminium foil (10 µm thickness) and dried at 70 °C for 12 hours. The electrodes have an area of ~1 cm² with mass loadings from around ~0.19 mg · cm⁻² of the total active carbon material. The electrodes were cast by doctor blade coating (Figure 2) dried

at 70 °C for around 24 h and subsequently were sandwiched using a cellulose paper filter as a separator.

2.3. Characterisation of materials

The sample BC and post-EMS activated carbon (BC6) were prepared using a gold coating (~5 nm) employing scanning electron microscopy (SEM) using JEOL JSM-5800LV at 15 kV coupled with energy dispersive X-ray (SEM/EDX) spectroscopy for determining the elemental composition. The spectroscopy analysis by FTIR and Raman and their surface functional groups of the samples were analysed by an Agilent Cary 630 Spectrometer FTIR (Fourier Transform Infrared Spectroscopy) within the range of 400-4000 cm⁻¹. The Raman spectra were estimated using JY Horiba Lab RAM HR using an excitation wavelength of 532 nm and laser power of 28 µW. The particle size distribution of BC samples in DMF was investigated using DLS (Malvern Zetasizer, Nano ZS Series) whilst the surface area was estimated by the multi-point Brunauer, Emmett and Teller (BET) method and complementing the BET analysis the BJH (Barrett, Joyner, and Halenda) method using Quantachrome Nova 1200e equipment. The crystal structure of BC samples was evaluated using a Siemens D5000 X-ray Powder Diffraction (XRD) System with Cu K α ($\lambda = 0.154$ nm). The XRD analysis was carried out under irradiation in the 2θ range of 20° to 80°. The chemical state of the BCo and BC6 samples were analysed using X-ray photoelectron spectroscopy XPS (Thermo-Scientific, EXCALAB Qxi).

2.4. Electrochemical measurements

Electrochemical performance tests using cyclic voltammetry (CV) were run on assembled supercapacitors (SCs) cells with active material weights within the range of 2.1 mg to 3.9 mg. Initial CV tests were run to evaluate the interaction of the black carbon (Bco) prior activation using choline chloride-based DESs (deep eutectic solvents) and a commonly used water-based electrolyte 0.1 M Na₂SO₄ (Aldrich, 99%), I (Aldrich, 99%) and DESs. The electrolytes choline-chloride based (hydrogen bond acceptor HBA) were prepared

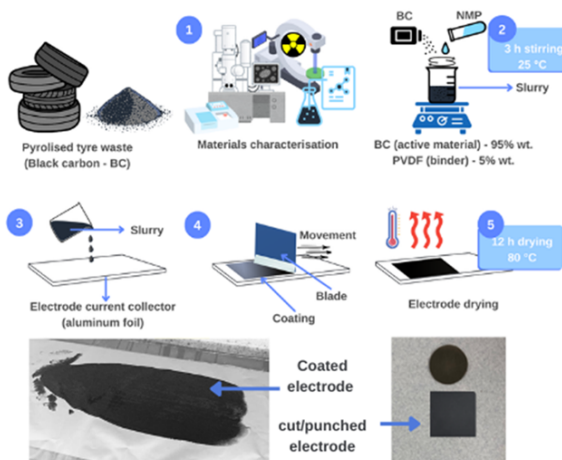


Figure 2: General scheme of the electrode design and preparation through doctor blade coating.

combining them with hydrogen bond donors (HBD). The electrolytes tested were ethaline 200 (ethylene glycol, Aldrich, 99.8%), oxaline (oxalic acid, Aldrich 98%) and glyceline (glycerine, Aldrich, 99%) were prepared according to the methods [5] Electrochemical measurements were conducted using a symmetric two-electrode supercapacitor setup. Given that both electrodes are identical and exhibit equivalent charge storage behaviour, the specific capacitance was determined by normalizing the measured capacitance to the active mass of one electrode (single electrode basis) [102, 49]. The electrochemical experimental data are used for calculating the specific capacitance according to the following equation based on the current response and the scan rate:

$$C_{sp} = \frac{\int I(V) dV}{2 \cdot v \cdot m \cdot \Delta V} \quad (1)$$

where $I(V)$ is the curve describing how current (A) varies with voltage (V) during voltammetry, v is the scan rate ($V \cdot s^{-1}$), m is the total mass of the active material in one?? electrode (g), and ΔV is the potential window (V).

A second round of CV was carried out to evaluate the electrochemical performance of the electrolyte against the activated carbon sample BC6 from the post-EMS activation process. The assembled supercapacitor with BC6 sample as active material was compared using ethaline 200 with other two electrolytes used in commercial electrolytes such as acetonitrile (Aldrich, 99%) and 0.6 M KOH (Aldrich, >85%). The electrochemical performances were evaluated in a two-electrode system (symmetric) using cyclic voltammetry (CV), galvanostatic charge-discharge (GCD) and electrochemical impedance spectroscopy (EIS) using an IviumStat electrochemical interface station. The electrochemical impedance spectroscopy (EIS) analysis was carried out by employing an amplitude of 5 mV over the frequency range from 0.1 Hz to 100 kHz.

3. Results and discussion

3.1. Materials characterisation

3.1.1. SEM images and EDS of surface elements of BC

Figure 3 displays scanning electron microscope (SEM) images of black carbon (Bco) and activated carbon powders before and after electrochemical molten salt (EMS) activation. A substantial alteration in surface structure is evident, with increased roughness and porosity in specific areas. Elemental analysis using EDS-SEM of the original Bco in Figure 3c revealed the existence of silicon (17%) and in Figure 3d sulphur (11%) distributed throughout the pyrolysed carbon particles. Sulphur is a prevalent contaminant in tyre waste, while silica is a widely utilised filler in rubber, providing cost-effective reinforcement due to its non-polar functional groups and hydrogen bonding with the elastomer [70]. Despite that sulphur is not the most desirable compound in a precursor of carbon-based materials, some literature has reported that sulphur can act as a highly efficient material for anodes in sodium-ion batteries and trigger more efficient

faradaic redox interactions happening in S-doped carbonaceous electrodes, leading to increased pseudocapacitance in supercapacitors [96, 59]. In the BC6 sample, the silica content rose to 27% in Figure 3e, while the sulphur content diminished to 6% in Figure 3f. Molten salt electrochemistry decreased the sulphur content in BC6 by 54%, presenting an alternative approach to desulfurisation.

3.1.2. BET analysis and DLS particle size distribution

Figure 4 illustrates the application of the BET equation to determine specific surface area using a multilayer adsorption model. The BET-estimated area for the Bco sample is $43.1 \text{ m}^2 \cdot \text{g}^{-1}$, while for BC6 post-EMS activation, it increases to $60.09 \text{ m}^2 \cdot \text{g}^{-1}$. This represents a 39.4% rise in apparent surface area, suggesting the formation of new porous structures on the carbon's surface [115]. The BJH method was employed as a supplementary technique to calculate an average pore volume of $0.23 \text{ cm}^3 \cdot \text{g}^{-1}$ and a pore size of 12.7 nm (127 \AA) for Bco, while for BC6, these values were $0.35 \text{ cm}^3 \cdot \text{g}^{-1}$ and 1.96 nm (19.6 \AA), respectively. The isotherms are of type II with a type H4 hysteresis loop in Figure 4a-b, characteristic of monocoat (monolayer)-multilayer adsorption in a network with mesoporous and microporous features typical of silt pores [39, 32, 40]. EMS activation method modified on the average value of the size of pores of the newly formed nanoporous, impacting the total surface area of BC6 available for adsorption and most notably, the size of molecules that can diffuse into the solid. Hence, the development of a suitable pore structure will affect the potential application of activated carbon [78, 15]. The type H4 hysteresis loop is also an indicator of meso-microporous structures in carbon materials like those found in mesoporous zeolites and silicas [95]. Adsorption sites play a key role in the SCs charging process as the accumulation of the electroactive species occupies the active sites of the carbon material whilst the surface diffusion of the adsorbed species will be distributed in the high surface area of carbon. Sulphur atoms create larger

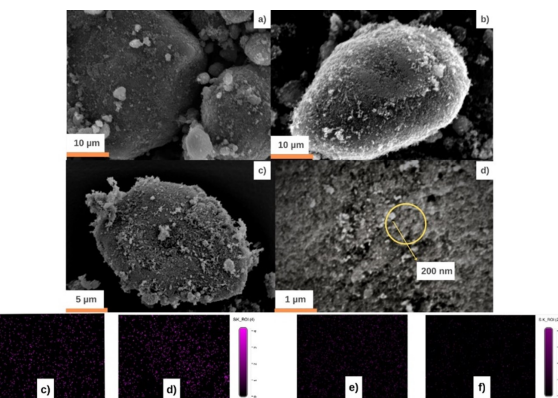


Figure 3: (a) Black carbon (Bco) prior activation by EMS. (b)-(c) Activated carbon by EMS (BC6). (d) Approximate pore diameter (200 nm) of BC6 sample. (c)-(d) EDS-SEM of Bco for Si-element and S-element. (e)-(f) EDS-SEM of BC6 (post activation by EMS) for Si-element and Si-element and S-element.

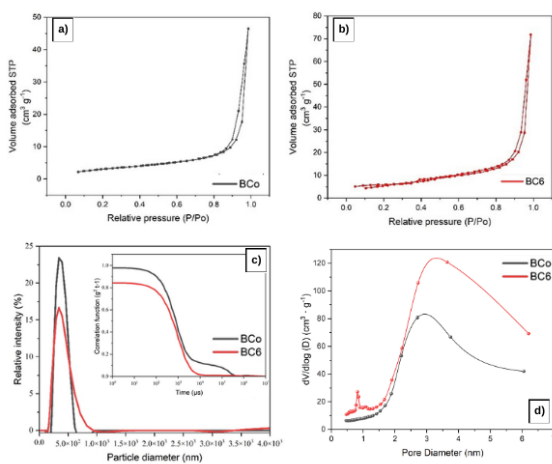


Figure 4: Black carbon (BCo) and activated carbon (BC6) surface analysis by: (a)-(b) BET adsorption isotherms. C) DLS particle size distribution and d) Pore size distribution curves.

interplanar distances in the micro and nanoporous structures. At the same time, sulphur is renowned for its high reactivity amongst heteroatom dopants due to its unpaired electrons (a polarizable character from a wider bandgap from an electron-withdrawing group) due to the subtle difference in electronegativity with carbon [96, 85, 92]. Electrochemical activation of recycled tyre waste into high-surface-area activated carbon offers a sustainable alternative to silica in carbon-based anodes. EMS process addresses the environmental issues associated with pyrolysed carbon, with an increased amount of silica (27% in BC6). By incorporating nanoscale silica into the activated carbon, this method enhances electrode performance by reducing stress, strain, and cracking, leading to increased reversible capacity [64, 43]. The repurposing of pyrolysed tyre waste minimises environmental harm, fosters sustainability, and aligns with the principles of a circular economy. By transforming discarded materials into valuable resources, the EMS approach reduces waste and creates new economic opportunities [44]. To determine the particle size of the carbon black (BC) particles before and after the electrochemical modification (EMS) process, dynamic light scattering (DLS) analysis was conducted. The results depicted in Figure 4c indicate that the activated carbon particles have an average diameter of 300 nm. However, the correlation function suggests a slightly faster decay, which is indicative of smaller particles exhibiting more rapid fluctuations in scattered light and a more rapid decline in the correlation function over time. Although there may not be a substantial change in particle size following EMS activation, some studies have observed a sharper peak, suggesting the potential presence of aggregated particles, a common occurrence in activation methods like carbonization or physical activation (e.g., steam activation) [95, 108]. In Figure 4d the pore size distribution plot characterises the porosity of materials by

showing the volume distribution of pores across different sizes by (BJH) method from nitrogen adsorption data. The BCo sample exhibits a dominant peak at ~2.5 nm, reflecting smaller mesopores, whereas the BC6 sample shifts to larger pore sizes (~3-4 nm) with a higher overall pore volume, aligning with its greater nitrogen adsorption capacity. These differences suggest structural modifications in BC6, making it potentially more suitable for applications requiring enhanced porosity, such as catalysis and adsorption that are also ideal for long-term energy storage because they share critical properties such as high surface area, tunable porosity, and chemical stability [42]. High surface area is essential for both catalysis, where it increases the number of active sites for reactions, and energy storage, where it enhances ion exchange and electron transfer, improving energy density and efficiency [42, 17]. Likewise, tuneable porosity cause by the EMS activation, as in the anode, the carbon atoms interact with various oxide ions adsorbed on the surface of the carbon material, resulting in the production of CO gas (Equations 2–3). The generation of both the ions and CO contributes to the formation of pores in the carbon surface, facilitating the efficient molecule trapping and release processes enabling fast ion diffusion and electrolyte access in batteries and supercapacitors [17, 13].



DLS assesses the size of particles suspended in a liquid by monitoring their random movement [13, 48]. The hydrodynamic size refers to the diameter of a hypothetical sphere that diffuses at the same rate as the particle of interest, with its intensity directly related to the particle's size [48, 113]. Mechanisms to get control over the forces that cause nanoparticles to cluster in a suspension are vital, as the system's behaviour can be influenced by electrostatic interactions, external fields, solvent characteristics, shape, and surface properties [103].

3.1.3. Analysis by FTIR, Raman, XRD and XPS spectroscopy

Raman spectroscopy was used to analyze the carbon structures of the samples, as illustrated in Figure 5a. The prominent D peak, located at approximately 1320 cm^{-1} , is a distinctive feature of carbonaceous materials with a disordered crystalline/amorphous sp³ structure, observable in both BCO and BC6 [75]. Conversely, in BC6, the G band at 1580 cm^{-1} arises from the stretching of sp² carbon atoms and reflects the degree of graphitization. This graphitization, characterised by cyclic and linear carbon structures, creates a porous matrix that can effectively retain and stabilize OPCM during phase transitions. The BC6 Id/Ig ratio of 0.83 indicates a high level of graphitization, which is further supported by an increase in surface area as demonstrated by BET analysis [98, 31]. In contrast, the BCo Id/Ig ratio of 0 suggests a disordered and defective carbon structure, similar to that observed in BC6 [31, 101]. It is reasonable

to conclude that the EMS process also contributes to the formation of highly porous structures with ordered sp₂ graphitic carbon, resembling graphite and other carbon-based materials known for their high thermal conductivity and low density [46, 114, 34].

The Fourier-transform infrared spectroscopy (FTIR) spectra in Figure 5b show the surface functional groups of carbon black (BC) before and after electrochemical modification (EMS). The broad peak observed at approximately 3450 to 3700 cm⁻¹ can be credited to carbon-hydrogen (C–H) and oxygen-hydrogen (O–H) functional groups. The peak at 3450 cm⁻¹ is a result of the stretching vibration of oxygen-hydrogen bonds from surface-adsorbed water [44, 114, 34]. The broad peaks observed between approximately 1200 and 1651 cm⁻¹ are associated with the stretching vibrations of the carbon-oxygen (C=O) and carbon-carbon (C–C) functional groups frequently found in tyre rubber waste and commercial carbon black. A broader peak is evident for Bco, while a more defined peak appears at 1651 cm⁻¹ for BC6, indicating the presence of the C=O group. The peaks within this range are attributed to the stretching frequency of the C=O bond, which was also intensified for BC6, suggesting that the oxygen content on the surface of BC6 is higher than that of Bco before EMS modification [114, 34]. The group of peaks located between 1970 cm⁻¹, 2026 cm⁻¹, and 2165 cm⁻¹ are due to the stretching vibrations of the (C≡C) group of carbon atoms in alkanes, alkyl groups, alkynes, and (N=C=S, SC≡N) groups in thiocyanates. The peak at 2165 cm⁻¹ is more prominent in BC6, resembling the characteristics of commercial carbon black N330 added to rubber, which increases the surface area and improves properties such as tear resistance, abrasion resistance, and elasticity in tyres, as documented in the literature. Conversely, the peak present at 750 cm⁻¹ corresponds to the C–S bond in the Bco sample but is absent in BC6, indicating the removal of sulfur after

EMS, similar to the peaks at ~1298 cm⁻¹ and ~1450 cm⁻¹ associated with the CH₃ stretching and methylene –CH₂ group bending. The lack of this peak directly correlates with the thermal oxidation of Bco and, consequently, the reduction of elastomer structural groups. The decrease in –CH₂ groups is directly linked to the breakage of C–S and S–S bonds, indicating a devulcanisation effect [8]. Studies related to the role of C–S have reported high-performance capacitive energy storage in Li-ion batteries and supercapacitors. In general terms, carbon materials possess non-polar C–C/C=C bonds and adding dopants like S, N or other functional groups on carbon surface enhanced surface polarity and materials with higher porosity are also favourable to capturing sulphur atoms [10, 20, 104]. On the other hands, silica was confirmed by the presence of a slightly elevated siloxane (Si–O–Si) peak at 1100 cm⁻¹ in both BC6 and Bco. Additionally, a peak attributed to Si–O bond stretching and silanol (Si–OH) was observed at 950 cm⁻¹ in Bco [19, 99]. It is remarkable to mention that the peak associated with Si–O groups is more prominent in BC6, which aligns with the increased silica content observed in the SEM-EDS analysis of the sample processed under EMS conditions.

XRD analysis shows in Figure 5c that both pyrolysis (Bco) and activation by EMS modified the crystalline structure of black carbon (BC6) derived from waste tyres. The narrower and taller (002) peak, indicative of enhanced graphitization, was observed in BC6 samples treated at 700 °C and 2.8 V for 2 hours during the EMS. The intensities of the (002), (101), and (004) diffraction peaks increased substantially in BC6 compared to Bco, implying a more organized arrangement of aromatic layers, a hallmark of carbon-based materials with carbon content exceeding 81% wt., such as coal [27], and those activated using both, heat treatments and enhanced by the electrochemical reactions [22, 35, 93]. The increased stacking of carbon can be attributed to the breakdown of aliphatic chains under heating conditions, which facilitates the condensation of aromatic rings and leads to their gradual expansion [42]. Furthermore, the presence of sulfur within the carbon matrix of the pyrolysed Bco samples contributes to the graphitization of carbon in BC6 when treated with chloride molten salt at temperatures below 700 °C (~675 °C). This makes the EMS activation method more energy-efficient than other thermal activation methods, as it does not require excessively high temperatures to promote the formation of crystallized graphite nanostructures [73, 82].

XPS analysis spectrum shown in Figure 5d confirms the presence of carbon I, silicon (Si), and oxygen (O). C1s spectrum with binding energy at 282 eV corresponding to metal carbide, in BC6 can be attributed to the development of Si–C bond. At the same time the presence of Si 2p and C1s spectra with the binding energy of ~100 eV and 282 eV associated with the vulcanized Si and C atoms of the SiC₁O₁ [93, 14]. Additionally, low-intensity peaks can be detected at ~260 eV corresponding to a C KLL Auger transition due to the ejection of a core-level electron (from the 1s orbital of carbon, or the K-shell of an Auger electron) by the incident X-rays, in this case, it represents a sp₂-hybridized

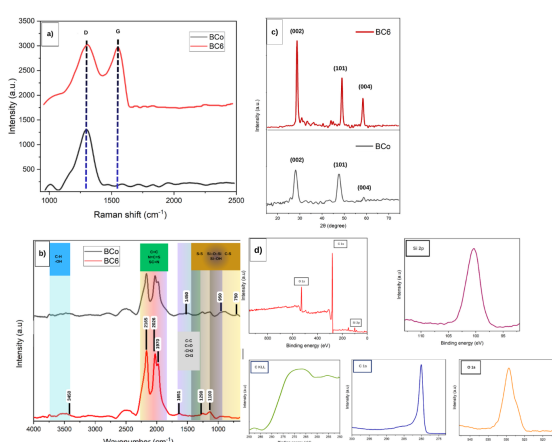


Figure 5: (a) Raman spectrum of black carbon (Bco) and post activation by EMS (BC6). (b) FTIR spectrum of Bco and BC6. (c) XRD pattern of Bco and activated carbon (BC6) after EMS. (d) XPS analysis of BC6 sample (C1s, O1s, C KLL and Si2p spectra).

Table 1

Specific capacitance estimated by CV on Bco (black carbon)

Electrolyte	Specific capacitance ($\text{F} \cdot \text{g}^{-1}$)
Na_2SO_4	13
Oxaline	3.44
Glyceline	2.15
Ethaline	16.33

carbon (C–C bond) that also suggesting some oxygenated functional groups from the activation process [14, 6]. The O1s spectrum exhibits a significant peak at 529 eV. The results of the C1s and O1s peaks suggested a C=O particularly when enhanced by molten salt activation [110, 69].

3.2. Electrochemical performance

The electrochemical properties of the electrodes prepared for each supercapacitor (SC) cell assembled with Bco and BC6 electrodes and their interaction with DESs based electrolytes were studied by cyclic voltammetry (CV) as is depicted in Figure 6. The electrochemical experimental data were used to estimate the specific capacitance using Equation 1.

In Figure 6 can be observed the cyclic voltammetry of the assembled electrodes in supercapacitor cells at a scanning rate of $100 \text{ mV} \cdot \text{s}^{-1}$ in a potential range of 0 to 1 V. The supercapacitors with Bco as active material (prior activation) were evaluated to estimate the interaction with different types of water-based electrolytes (0.1 M Na_2SO_4) and DESs (ethaline 200, oxaline and glyceline) for Bco (Figure 6a). The specific capacitances are shown in Table 1.

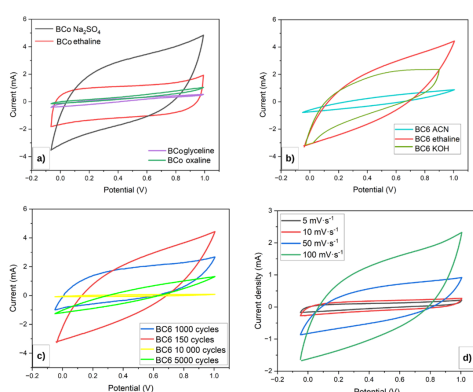


Figure 6: a) CV of Bco (black carbon) with water-based electrolytes (Na_2SO_4) and DESs (ethaline, glyceline, oxaline). b) CV of BC6 (activate carbon) against I, KOH and ethaline electrolytes. c) CV of BC6 against ethaline 5 cycles (red), 150 cycles (blue), 1000 cycles (green) and after 10 000 cycles (yellow). d) Scan rates of ethaline with BC6 at $5 \text{ mV} \cdot \text{s}^{-1}$, $10 \text{ mV} \cdot \text{s}^{-1}$, $50 \text{ mV} \cdot \text{s}^{-1}$ and $100 \text{ mV} \cdot \text{s}^{-1}$.

The cyclic voltammetry experiments revealed that the BC exhibited conductive behaviour when tested with conventional electrolytes like Na_2SO_4 , as well as eco-friendly alternatives known as deep eutectic solvents (DES). These green electrolytes offer characteristics that can enhance the energy storage capabilities of the supercapacitor [38]. Water-based electrolytes offer several advantages for supercapacitors, with Na_2SO_4 being one of the most commonly used options. It provides a neutral pH environment, which helps minimise corrosion and extends the lifespan of both the electrodes and current collectors. Moreover, research has shown that Na_2SO_4 can operate within a voltage range of 1.23 V to 1.6 V, surpassing the typical 1.2 V limit imposed by water electrolysis. This ability to function at higher voltages contributes to improved energy density while maintaining the stability of both the electrolyte and the electrodes [53, 45]. Despite its high ionic conductivity, minimising the internal resistance in the supercapacitor, considering the interaction with the black carbon, Na_2SO_4 is conductive as it can be observed, but it tends to be competitive with other aqueous systems, helping supercapacitors achieve excellent cycling stability and efficiency. The nature of the black carbon from plastic waste, suggests that the Bco electrode doesn't possess the surface wettability required to promote the charge-transfer process and electrode-electrolyte interactions [51, 57]. Building on this, a DES solvent known as ethaline 200, made from a 1:1 ratio of choline chloride and ethylene glycol, was utilised alongside oxaline and glyceline. Deep eutectic solvents (DESs) are defined as eutectic mixtures composed of Lewis or Brønsted acids and bases, typically in the form of organic salt solutions. These solutions often include choline chloride (a quaternary ammonium salt) combined with a hydrogen bond donor (HBD) molecule, such as ethylene glycol, urea, or glycerine, in a specific molar ratio. This unique pairing creates a mixture with a eutectic melting point significantly lower than the melting points of the individual components [24].

Ethaline is a mixture of quaternary ammonium salts mixed with metal salts or hydrogen bond donors (HBDs) choline chloride normally and ethylene glycol which have been applied in many areas including electrodeposition of metals and alloys. Ethaline provides several advantages such as high electrochemical stability, low volatility, and wide potential windows. DES is promising as an alternative to aqueous and organic electrolytes, especially in high-performance supercapacitors [68]. Choline chloride is considered a very low acute oral toxic which makes DESs easy to prepare, non-volatile, biodegradable, insensitive to water, and recyclable, all of which make their use in large-scale applications highly beneficial [35, 41]. Ethaline was selected as the electrolyte for further studies on BC6 (activated carbon by EMS), as it exhibits a more stable and behaviour close to the ideal rectangular shape of voltammograms also with largest area which means the formation of an electric double layer [79].

In contrast, oxaline and glyceline were prepared following the method outlined in [56]. Both exhibit higher viscosities compared to other organic-based electrolytes like ethanol or

Table 2

Specific capacitance estimated by CV on BC6 (black carbon)

Electrolyte	Specific capacitance ($\text{F} \cdot \text{g}^{-1}$)
ACN	17.79
KOH	214.7
Ethaline	110.16

acetonitrile; however, they also demonstrate greater conductivity due to their relatively lower viscosities. Oxaline-based DESs, with conductivities ranging from 1 to $10 \text{ mS} \cdot \text{cm}^{-1}$, experience slower ion diffusion and mobility because of the presence of strong hydrogen bonding. This property limits their suitability for fast electrochemical reactions but proves advantageous in applications requiring controlled ion transport. Glyceline, on the other hand, shows conductivities between 0.1 and $5 \text{ mS} \cdot \text{cm}^{-1}$ and similarly exhibits high viscosity due to the polyol structure of glycerol, which promotes extensive hydrogen bonding. This viscosity can be mitigated by increasing the temperature, as the improved fluidity enhances ion mobility and as a consequence, glycerine conductive performance [35, 56, 58, 112]. However, despite the evaporation is minimal which benefits in supercapacitor applications, as can be observed in the CV test, both don't interact efficiently with the designed electrode because of their properties that make them less favourable for applications requiring rapid ion transport. Nonetheless, their characteristics, such as higher viscosity and slower ion mobility, make them well-suited for applications where controlled ion transport is preferred, such as in biocatalysis or controlled-release systems [35, 56].

Conversely, in Figure 6b the sample BC6 (activated carbon post-EMS process) showed the highest specific capacity keeping the rectangular CV shape, showing a higher double-layer capacitance effect. BC6 electrochemical performance by CV was compared using ethaline 200, acetonitrile (I) and 0.6 M KOH as an electrolyte. The results are described in Table 2.

As can be observed in Figure 6b and Table 2, the interaction between BC6 as active material in the electrodes suggests and improved electrochemical behaviour with water-based electrolytes (KOH) rather than organic electrolytes commonly employed to widen the voltage window, improving energy density. However, the main reason why some organic solvents aren't able to act as efficient electrolytes is due to their difference in polarity which varies the ion conductivity of the electrolyte [58]. The nature of activated carbon is abundant oxygen-containing functional groups (e.g., hydroxyl, carboxyl, and carbonyl groups), which are more hydrophilic. Organic solvents, specifically non-polar or weakly polar ones like acetonitrile or propylene carbonate, seem not to wet the activated carbon surface efficiently [105]. Building on this, there is a significantly effect on the poor wettability?? resulting in the inefficient electrolyte penetration of the electrolyte into the porous structure of activated carbon,

reducing the available surface area for charge storage and dropping the overall capacitance of the SC. In contrast, some studies show that a mixture of alkaline or acidic chemicals can contribute to a better performance of supercapacitors, like diluted KOH. Favourable solvent-electrode interactions in water-based electrolytes also influence the stability and durability of the SC, as the water molecules facilitate the maintenance of the structural integrity of the activated carbon during charge-discharge cycling. Under this framework, the main challenge to overcome in the use of aqueous-based electrolytes is their narrow electrochemical stability window (~1.23 V). This constraint restricts the energy density of supercapacitors using aqueous electrolytes, in comparison with organic solvent-based systems, which can operate at higher voltages (2.5-3 V) [79]. Nevertheless, KOH-based electrolyte plays an important role in the industry in total dependence of the applications especially those where high-power density and cycle life are prioritised.

On the other hand, is remarkable to mention that a specific capacitance of $110.16 \text{ F} \cdot \text{g}^{-1}$ for ethaline, possesses a visible efficiency and stability with the BC6 electrodes. Polar nature of ethaline owing to the presence of both choline chloride and ethylene glycol, allows the formation of strong hydrogen bonds [114, 119]. Activated carbon typically contains a variety of oxygen-containing functional groups on its surface, such as hydroxyl, carbonyl, and carboxyl groups. These groups facilitate the formation of hydrogen bonds or electrostatic interactions with the choline chloride and ethylene glycol components of ethaline. The activated carbon produced through EMS activation, as illustrated in Figure 6d using XPS analysis, displays distinct C1s and O1s peaks, indicating the presence of C=O groups, particularly when molten salt activation is employed. Additionally, since Ethaline evaporates much more slowly compared to organic or water-based electrolytes, it can support extended cycling periods, as demonstrated in Figure 6c.

It is remarkable to mention that the CV shows consistent behaviour over 150 cycles, closely resembling the trend observed up to 1000 cycles, corresponding to a capacitance retention of approximately 55.5% ($61.11 \text{ F} \cdot \text{g}^{-1}$). Additionally, it is important to note that after 1000 cycles, supercapacitors typically experience failures due to electrolyte evaporation. However, tests with ethaline indicate that it retains a portion of the ELDC effect, valuable insights for further optimisation of long-life supercapacitors. This could potentially be achieved through alternative configurations, such as hybrid or asymmetric supercapacitors. The specific capacitance to a capacitance retention of approximately 44.7% after 5000 cycles ($49.24 \text{ F} \cdot \text{g}^{-1}$), highlighting the challenges of long-term stability and underscoring the need for improved electrolyte formulations or structural designs to mitigate capacitance loss [45]. Based on the measurements presented in Figure 6d, at 150 cycles the maximum value of the specific capacitances was calculated to be around $110.16 \text{ F} \cdot \text{g}^{-1}$ in the range of scan rate of $100 \text{ mV} \cdot \text{s}^{-1}$, showing that ethaline electrolyte shows a well-defined, relatively rectangular-shaped CV curve. This indicates that the capacitor is operating with minimal

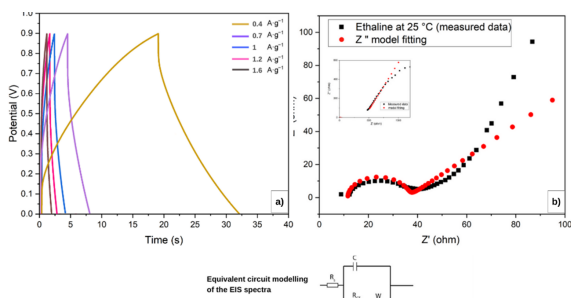


Figure 7: a) Galvanostatic charge-discharge profiles at different current densities of BC6 electrodes with ethaline as electrolyte at different current densities. b) EIS Nyquist Plot and circuit modelling for BC6 and ethaline as electrolyte at room temperature.

resistance and exhibits a good electrochemical double layer capacitance (EDLC) behaviour, where the ions are able to move quickly to form a charge layer at the electrode surface. At higher scan rates, like $50 \text{ mV} \cdot \text{s}^{-1}$ and $100 \text{ mV} \cdot \text{s}^{-1}$, the performance is more representative of practical, real-world supercapacitor behaviour, where faster charge/discharge is needed.

The current response in CV is highly dependent on the scan rate, which can complicate the accurate extraction of specific capacitance, especially when non-ideal behaviours in or Faradaic reactions are involved, especially in this case was the interaction between a new material developed as BC6 using ethaline as electrolyte [89, 12]. Galvanostatic Charge and Discharge (GCD) is suitable for evaluating energy storage devices' performance under practical charging conditions. Combining (GCD) with Electrochemical Impedance Spectroscopy (EIS) provides a powerful method to study the electrolyte-electrode interactions in electrochemical systems. EIS contribute to the understanding of key parameters like electrolyte resistance, double-layer capacitance, and charge transfer resistance [89, 23, 2, 107]. GDC and EIS analysis were carried out as it is shown in Figure 7.

GDC electrochemical data were collected and calculated using the equation The equation to calculate the specific capacitance C_{sp} n Farads per gram ($\text{F} \cdot \text{g}^{-1}$) from electrochemical data for symmetric supercapacitor is described below [26] :

$$C_{sp} = \frac{4I}{m \cdot (dV / dt)} \quad (4)$$

where I is the constant current applied during the GCD process (A) and m is the mass of the active material (g). In order to evaluate the electrochemical performance of the BC6-ethaline supercapacitors (SCs), galvanostatic charge-discharge (GCD) measurements were conducted at different current densities. The current densities were calculated with the mass of active material mass loading of $0.19 \text{ mg} \cdot \text{cm}^{-2}$ and the voltage of 1 V to avoid potential water electrolysis. The BC6 electrode demonstrated a near-ideal triangular profile with a specific capacitance of $92.2 \text{ F} \cdot \text{g}^{-1}$, indicating predominantly electric double-layer capacitance (EDLC)

behaviour, as corroborated by the cyclic voltammetry (CV) results. Moreover, its longer discharge times at comparatively higher current densities, relative to other supercapacitors fabricated with activated carbon, highlight the influence of factors such as the source of the carbon, activation method, electrolyte concentration, and surface area. For instance, activated carbon derived from biomass can achieve specific capacitance values of approximately $195 \text{ F} \cdot \text{g}^{-1}$ at a current density of $0.5 \text{ A} \cdot \text{g}^{-1}$ when activated via pyrolysis using 10% KOH as the activating agent [107, 91]. Similarly, another study reports that pyrolysed black carbon from waste tyres exhibits a specific capacitance of $212.2 \text{ F} \cdot \text{g}^{-1}$ at $1 \text{ A} \cdot \text{g}^{-1}$, with a surface area of $690.9 \text{ m}^2 \cdot \text{g}^{-1}$, using a $1 \text{ M Et}_4\text{NBF}_4/\text{AN}$ organic electrolyte [91]. However, the presence of sulfur in the carbon generated during pyrolysis can limit its applicability in supercapacitors. Sulfur bonds are essential for maintaining the physical and chemical stability of rubber under environmental conditions, but breaking these bonds through devulcanisation is both costly and energy-intensive. This process requires significant amounts of chemicals and energy, making it impractical for large-scale upcycling of black carbon from tyre pyrolysis, and thus it has not been widely adopted [79].

On the other hand, developing carbon-based materials with high specific surface areas and optimised pore structures, particularly medium-sized pores (mesopores), is vital for improving the efficiency and longevity of energy storage systems. Post-recycling activation methods, such as potassium hydroxide (KOH) impregnation, are frequently used to enhance the formation of mesopores. For instance, one study demonstrated an increase in surface area to $115.2 \text{ m}^2 \cdot \text{g}^{-1}$, achieving a specific capacitance of $218 \text{ F} \cdot \text{g}^{-1}$ [56]. Although this surface area nearly doubles that obtained for BC6 after EMS treatment, it is evident that, beyond porosity, factors such as electrode configuration and the interaction with electrolytes significantly influence supercapacitor performance [114].

The role of mesopores (2-50 nm in diameter) is particularly critical. These pores balance surface area and pore volume, enabling efficient ion transport and fast diffusion within the electrode. Mesopores provide a large surface area for ion adsorption, boosting overall energy storage capacity. At the same time, their size ensures easy access for electrolyte ions, enhancing the interaction between the electrolyte and the electrode material [58]. Furthermore, mesopores improve the structural stability of the electrode, reducing the risk of long-term degradation [112]. This balance between energy density and power density enables both high-charge storage and rapid energy delivery. Considering these attributes, the BC6 electrodes' performance in energy storage devices, specifically their energy density and power density, hinges on the interplay between material porosity, electrolyte interaction, and electrode architecture.

Considering these features, the BC6 electrodes demonstrate remarkable energy storage performance. Energy and power densities were calculated based on the total active mass of both electrodes in the symmetric device reaching an energy

density of $12.50 \text{ W} \cdot \text{h} \cdot \text{kg}^{-1}$ and a higher power density of $2.25 \text{ kW} \cdot \text{kg}^{-1}$ respectively. These results reflect lower energy density and a similar power density when compared to previously reported values for activated carbon electrodes derived from tyre waste in hybrid supercapacitors (e.g., $4.7 \text{ W} \cdot \text{h} \cdot \text{kg}^{-1}$ and a maximum power density of $6362.6 \text{ W} \cdot \text{kg}^{-1}$) [74]. This difference underscores the critical role of supercapacitor configuration and the interactions between its components (especially influenced by the electrode-electrolyte interaction) in influencing overall device performance. This can be explained by a multi-level porous framework with extensively branched and interlinked voids reflected in the increased surface area of BC6 of the BET analyses and supported by the disorder of the graphitic structure presented in the XRD analysis and Raman spectroscopy. Pores at various length scales shorten the ion diffusion pathways, promoting increased diffusivity through the interlinked voids resulting in a more efficient electrode material-electrolyte electric double layer effect to fully utilize the electrode capacity, ultimately enhancing the energy density and power density [58, 105].

Alternatively, EIS Figure 7b indicates excellent capacitive behaviour of the supercapacitor assembled with BC6 activated carbon by EMS. It can be observed by low charge transfer resistance, minimal solution resistance, and efficient ion diffusion, attributed to the porous structure of activated carbon. The presence of Warburg impedance (W) reflects the electrolyte diffusion at the electrode surface, confirming a positive interaction between the BC6- EMS electrochemically activated carbon and ethaline. Although high-energy-intensive methods, such as tyre pyrolysis or microwave activation, can produce specific surface areas between $800 \text{ m}^2 \cdot \text{g}^{-1}$ and over $2000 \text{ m}^2 \cdot \text{g}^{-1}$ ([26]) significantly higher than the $\sim 60 \text{ m}^2 \cdot \text{g}^{-1}$ achieved by BC6 after EMS, however, the plot's proximity to the origin suggests and a steeper line of the circuit model in the curve, which signifies the capacitive behaviour of the SCs [89]. This fact reflects low solution resistance (R_s), characteristic of ideal capacitive behaviour, and a small semicircle in the high-frequency region, suggesting low charge transfer resistance. The equivalent circuit model provides an excellent fit, indicating that the observed impedance behaviour arises from a combination of solution resistance, charge transfer resistance, electric double-layer capacitance, and ion diffusion within the pores of the BC6 activated carbon [12]. At the same, the lower viscosity of ethaline (in comparison with the other DESs studied) and the molecular structure ensure good wettability of the electrode surface. This behaviour is characteristic of systems with efficient electrolyte diffusion across the surface of the supercapacitor, minimising resistance at the electrode-electrolyte interface [112, 84]. The small semicircle observed in the charge transfer resistance (R_{ct}) region indicates a highly efficient charge transfer process, which aligns with the energy storage mechanism in supercapacitors, dominated by electric double-layer capacitance rather than faradaic reactions and ensuring an intimate contact between the electrolyte and the electrode, minimising impedance at the electrode-electrolyte interface. The enhanced surface area of BC6 compared to the

original Bco reduces overall system impedance by increasing capacitance in the low-frequency region and lowering charge transfer resistance [115, 2, 7].

4. Deep learning analysis

Machine learning models can be thought of as universal function approximators. That is, provided enough data to learn from, they are able to model any continuous, closed domain function to an arbitrary degree of accuracy [29]. Such models consist of interconnected “neurons” arranged in layers. These connections are dense, meaning each neuron is connected to all other neurons in the previous and next layer, giving rise to the common “fully connected” layer terminology. We will refer to a single layer as $F_i^{n,m}$ where i is the position of the layer, n is the input size (the number of input neurons expected), and m is the output size. The layer computes:

$$\hat{y} = F_i^{n,m}(x) = W_i x + b_i \quad (5)$$

where x is an n -dimensional vector, \hat{y} is an m -dimensional vector, W_i is an $n \times m$ weight matrix and b_i is a constant term. Layers may be chained sequentially, as long as the inner dimensions of adjacent layers are equal, i.e. W_i and W_{i+1} can be multiplied. Such a sequence of connected layers is commonly referred to as a Multilayer Perceptron (MLP). An important element of the layers of the MLP is the activation function, which is applied to the output of each neuron, and introduces non-linearity into the model. This is essential for an MLP to fit the definition of a universal function approximator as defined earlier, because any sequence of fully connected layers must necessarily collapse into a single linear transform, which is not powerful enough to represent more complicated functions. The Rectified Linear Unit function (ReLU) is a popular activation function [3] designed for this purpose and is defined as follows:

$$\text{ReLU}(x) = \begin{cases} 0 & x \leq 0 \\ x & x > 0 \end{cases} \quad (6)$$

Thus, the MLP must have a ReLU activation function between each hidden layer, giving the final model structure as laid out in Figure 8. Obtaining a \hat{y} prediction from an MLP completes the “forward pass” part of training. The prediction is then evaluated against the target value y (also called the ground truth value) using a cost function L – see Equations 11 - 14 for how it is defined for this application. The partial derivative of L is calculated with respect to each parameter $w_i^{n,m}$ in W_i :

$$\frac{\partial L}{\partial w_i^{n,m}} = \frac{\partial L}{\partial \hat{y}} \cdot \frac{\partial \hat{y}}{\partial w_i^{n,m}} \quad (7)$$

Computing all such partials completes the “backwards” pass of the training step – a process known as backpropagation

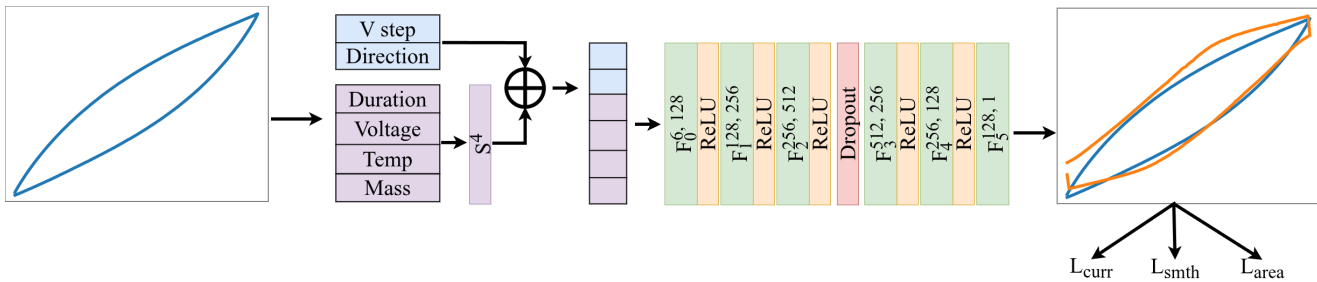


Figure 8: An overview of the training pipeline and model architecture, incorporating dropout after the largest layer to discourage overfitting. The input is a 6-dimensional vector consisting of a potential step, scan direction, and several experimental conditions under which the electrode material was synthesised; the output is a prediction of the current value at that potential. Four trainable weights S^4 provide a scaling factor for each of the conditions. Ground truth hysteresis curves shown in blue and model prediction shown in orange.

– and gives us $\frac{\partial L}{\partial W_i}$, which tells the model how much, and the direction in which W should change in order to minimise L . Repeating these forward and backwards passes over the MLP over and over again brings the weights closer to their “ideal” values – ones for which L is minimised. In other words, the optimising algorithm uses the difference between the output of the model and its target to update W in the correct direction. This is what is meant by training a machine learning model.

4.1. Previous work

The application of machine learning systems to the prediction of specific capacitance values is varied – some previous investigations involve predicting specific capacitance directly from experimental conditions [55], while others use these experimental conditions to predict hysteresis curves [76]; the latter approach allows the indirect calculation of specific capacitance C_{sp} , which is proportional to the area between charge and discharge curves. It is this latter approach that is used by the present study, because predicting the full charge-discharge dynamics of cyclic voltammetry allows the model to generalise better to a wider range of conditions [18] – especially important given the limited data available for this study. Using this approach, C_{sp} is given by Equation 1, where $I(V)$ refers to the function that is approximated by the MLP.

4.2. Dataset

The complete dataset comprises current samples from five cyclic voltammetry cycles, labelled BC2, BC3, BC5, BC7, and BC9 (see Table 3). Two cycles, BCo and BC6, were excluded from the analysis. BCo corresponds to untreated raw black carbon, prior to molten salt electrolysis, and was therefore not comparable to the processed samples considered in this study. BC6 was excluded due to its status as a pronounced outlier in specific capacitance, exhibiting a value approximately an order of magnitude larger than the remainder of the treated samples, despite only modest differences in experimental conditions. Given the limited number of unique feature configurations in the dataset, inclusion of this sample would exert disproportionate influence on model optimisation and obscure trends observed in the remaining, internally consistent cohort.

Table 3

Experimental conditions that were used during the synthesis of the electrodes, and ground truth C_{sp} values for each cycle. Data from all cycles were captured at a scan rate of $100 \text{ mV} \cdot \text{s}^{-1}$, and an ethaline electrolyte was used in the cell. † indicates cycles that were not included in the ML analysis.

Cycle	M / mg	T / °C	D / h	V_e / V	C_{sp} / F · g ⁻¹
BCo [†]	0.08	-	-	-	16.33
BC2	0.11	800	2	2	17.92
BC3	0.11	750	2	2	21.55
BC5	0.18	650	2	2	27.04
BC6 [†]	0.20	700	2	2.5	110.16
BC7	0.25	700	2	2.8	10.60
BC9	0.25	750	2	2.8	8.477

All data were collected via potentiostat with a scan rate of $100 \text{ mV} \cdot \text{s}^{-1}$. Each cycle consists of 264 rows, with columns for current (I / A), voltage step (V / V), active electrode mass (M / mg), temperature (T / °C), electrolysis duration (D / h), electrolysis voltage (V_e / V), and scan direction (S). The last feature tells the model if the particular point is on the charge or discharge curve and is represented by either +1 (charging) or -1 (discharging).

Notice that the various inputs span many orders of magnitude – this is a problem for machine learning models. Using raw features such as those presented in Table 3 mean that ones with large absolute values dominate the weights of the model, even though they may not be as important, and vice versa, which can lead to lower performance [54]. For this reason, all features are scaled across all cycles such that they have zero mean and unit standard deviation. To transform an individual instance of a feature d_i (e.g. electrode mass, temperature) to its scaled value $d_{norm,i}$:

$$d_{norm,i} = \frac{d_i - \mu(D)}{\sigma(D)} \quad (8)$$

where D is the collection of all the values for this feature, μ is the mean of values in D , and σ is their standard deviation.

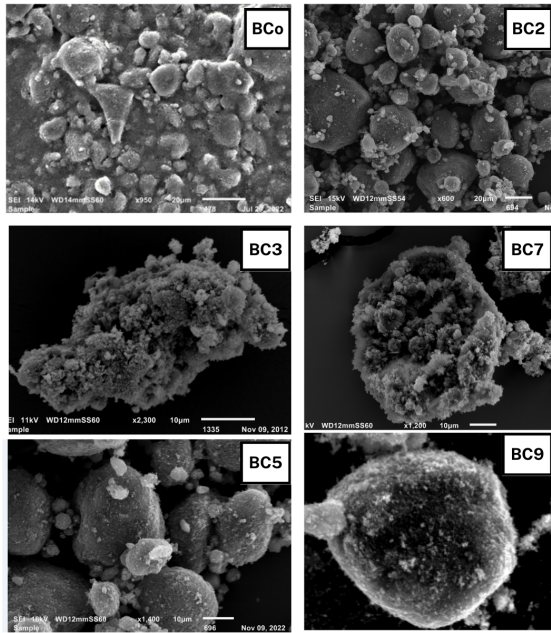


Figure 9: SEM scans of the molten salt treated BC materials used for each of the cycles. BC0 is the untreated black carbon material.

These scaled values are used in all subsequent machine learning operations, and final outputs are de-normalised using the inverse of Equation 8 for display and comparison with experimental values. Current values were also transformed in this way. However, the potential step V was rescaled slightly differently: rather than ensuring zero mean and unit variance, we rescale them such that the minimum potential across the whole dataset is -1 and the maximum is +1:

$$\begin{aligned} V_{mid} &= \frac{V_{max} + V_{min}}{2} \\ V_{half-range} &= \frac{V_{max} - V_{min}}{2} \\ V_{norm} &= \frac{V - V_{mid}}{V_{half-range}} \end{aligned} \quad (9)$$

where V_{min} and V_{max} are the minimum and maximum potential values *across the whole dataset*. This scaling ensures that all cycles share a common and bounded potential domain, making it easier for the model to learn consistent relationships across different experimental conditions.

The input to the model is therefore a 6 dimensional, normalised feature vector that consists of a potential step and experimental conditions under which the electrode material was synthesised, and the output is the current value at the potential step.

4.3. Experimental design and model architecture

We employ leave-one-out cross validation when training: for any one run, the model is trained only on points from 4 of the cycles; points from the 5th are held out for validation. Here, validation means only evaluating the forward pass of

the model and not updating the weights of the model. It is a test to determine if the model is able to generalise to “unseen” data, and each cycle is subjected to this treatment in turn. We repeat training runs five times independently to build confidence that the model’s output is reliable, and report the average in all subsequent results.

Due to the small size of the dataset, we introduce a simple heuristic to improve the training stability and to encourage the model to learn meaningful relationships between experimental conditions and the voltammetric response. This is realised by introducing four trainable parameters that act as scaling factors for the experimental conditions that are used when synthesising the black carbon – active mass (M), electrolysis temperature (T), electrolysis duration (D) and electrolysis voltage (V_e). These parameters allow the model to explicitly learn the relative importance of each condition rather than solely relying on implicit weighting within the first layer of the MLP.

As illustrated in Figure 8, the learned scaling parameters S^4 are applied to the condition vector prior to concatenation with the potential step (V) and scan direction (S), resulting in the 6-dimensional input that is expected by the MLP. Scaling is applied in the following way: the learned weights are first divided by a temperature parameter τ , which controls the sharpness of the relative weighting, and subsequently normalised by the softmax function [9] to give the scaling factor f_i for each learned weight:

$$f_i = \frac{\exp(s_i/\tau)}{\sum_{j=1}^4 \exp(s_j/\tau)} \quad (10)$$

where s_i is any one of the four learned weights. The resulting normalised weights are multiplied element-wise by the condition vector, yielding the weighted condition vector.

The rest of the model is a multilayered perceptron with 4 hidden layers in between a 6-neuron input layer and a 1-neuron output layer. Please refer to Figure 8 for the full model architecture. Note the dropout layer, which randomly (with some probability p) deactivates a subset of neurons during training. This is done so that the model does not rely too heavily on any single neuron or set of neurons, thereby reducing overfitting and improving generalisation to new data [65]. Wider layers with more neurons benefit more from dropout as they are more at risk from overfitting [94], hence the placement between F_2 and F_3 .

As mentioned in the Section 4, the objective function scores the output of the MLP so it can be used in gradient calculations, which in turn are used to inform updates to the model’s weights. Because the model predicts the current at a particular voltage step, part of the loss function is the mean squared error (MSE) between the predicted and actual value. This is given by:

$$L_{curr} = \frac{1}{N} \sum_{i=1}^N (\hat{y}_i - y_i)^2 \quad (11)$$

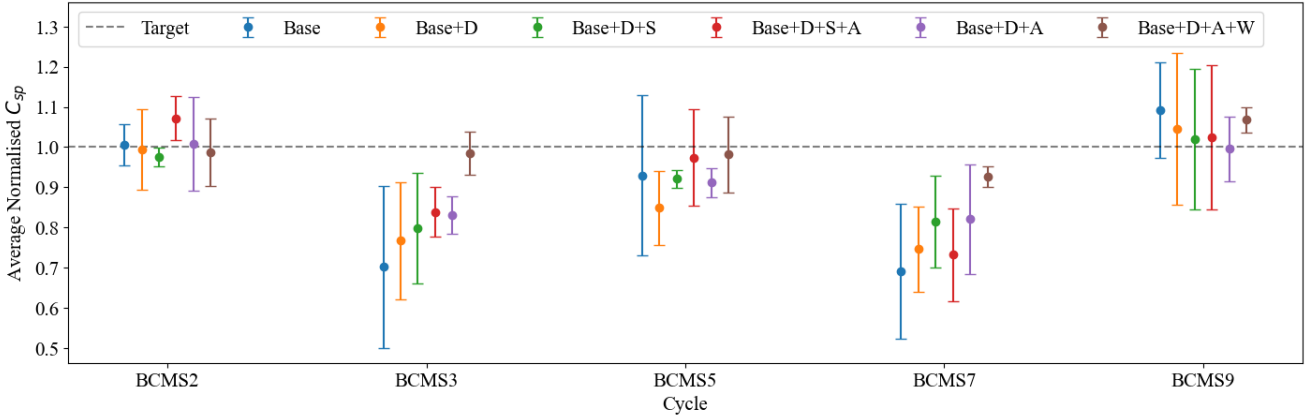


Figure 10: A plot reporting the average normalised C_{sp} over 5 runs per cycle per experimental setting. Error bars indicate 95% confidence intervals over runs.

where \hat{y}_i is the predicted current value, y_i is the true value, and N is the number of predicted points. Further, in order to maintain a smooth curve that is physically consistent with the behaviour of real hysteresis curves, we impose a penalty on the second derivative of the predicted current with respect to potential, discouraging sharp local curvature and jitter:

$$L_{smth} = \left\| \frac{\partial^2 I_{pred}}{\partial V^2} \right\|_2^2 \quad (12)$$

where I_{pred} is the predicted current and V is the potential. Finally, we also use the area of the predicted curve in another MSE loss calculation to encourage the model to produce the correct net area exhibited by the experimental curve:

$$L_{area} = \frac{1}{M} \sum_{j=1}^M (\hat{a}_j - a_j)^2 \quad (13)$$

where M is the number of cycles, a_j is the actual area between the curves for a given cycle, and \hat{a}_j is the area calculated using predicted current values. The losses are combined for final objective for the MLP:

$$L = L_{curr} + L_{smth} + L_{area} \quad (14)$$

In order to assess the importance of these loss functions (as well as other model settings), an ablation study was conducted to measure the impact these settings on the final prediction. A comparison of C_{sp} predicted by models under these experimental settings is given in Figure 10, and a comparison of their relative errors is given in Table 4. The base MLP, henceforth called “Base” is only tasked with the L_{curr} objective. The following experimental modifications were added to the Base model:

1. “+ D” – inclusion of a Dropout layer, as discussed in Section 4.3
2. “+ S” – addition of the Smoothing L_{smth} objective to L
3. “+ A” – addition of the Area L_{area} objective to L
4. “+ W” – inclusion of trainable Weights for each of the synthesis conditions

Table 4

Average error (relative %) for each cycle in leave-one-out cross validation over 5 independent runs. Base+D+A exhibits the least overall error across all the settings.

Cycle	Base	Base +D	Base +D +S	Base +D +S+A	Base +D +A	Base +D +A+W
BC2	0.62	0.58	2.54	7.17	0.77	1.22
BC3	29.82	23.28	20.15	16.11	16.93	1.53
BC5	7.04	15.05	7.88	2.61	8.83	1.77
BC7	30.87	25.37	18.50	26.78	17.92	7.42
BC9	9.12	4.64	1.91	2.42	0.39	6.83
Average	15.49	13.79	10.20	11.02	8.97	3.75

4.4. Results and discussion

Results were collected for each experimental setting described in Section 4.3. Figure 10 demonstrates the averaged, normalised C_{sp} values computed over five independent runs. Predicted C_{sp} were normalised by their corresponding ground-truth values to facilitate comparison across settings. Error bars indicate the 95% confidence interval over the five runs. Tables 4 and 5 report results for each leave-one-out fold, where the Cycle column indicates the curve that was left out.

Overall, the Base+D+A+W configuration (corresponding to the model incorporating dropout, condition scaling, and the area loss of Equation 13) exhibits the smallest deviation from the C_{sp} baseline, on average. This setting also yields comparatively narrower confidence intervals, suggesting improved stability across runs. Incorporating the area-based loss term resulted in improved performance across all curves. As shown in Figure 10, models that include this loss term tend to produce predictions that are closer to the target baseline. It should be noted that the smoothness loss term (Equation 12) seems to be somewhat at odds with the area loss. This effect is reflected in Table 4, which presents the relative error percentage between the predicted and true C_{sp}

Table 5

Relative weights assigned by the proposed model to the various molten salt parameters. The exclusion of one curve from each training run under our leave-one-out regime gives a slightly different set of weights for each experiment. Overall, the model was most sensitive to temperature (T), electrolysis voltage (V_e) and active mass (M). Electrolysis duration (D) was found to be the least important input in predicting C_{sp} .

Cycle	M	T	D	V_e
BC2	0.193	0.294	0.173	0.339
BC3	0.266	0.264	0.237	0.233
BC5	0.254	0.285	0.175	0.286
BC7	0.223	0.301	0.202	0.275
BC9	0.214	0.413	0.170	0.203
Average	0.230	0.311	0.191	0.267

values across all the experimental settings. The addition of area loss to Base+D+S (10.2% error) results in the error increasing slightly to 11.02%. Removing the smoothness loss (corresponding to the Base+D+A configuration) yields a lower overall error (8.97%). This suggests that the two loss terms may impose competing constraints on the learned representations, which could partially limit their combined effectiveness. However, the most effective strategy incorporates condition scaling to the latter configuration (giving Base+D+A+W), and yielding an average error of 3.75%.

The inclusion of trainable scaling values for the four experimental conditions (M, T, V and D) offers insights into the relative importance of each of these in determining C_{sp} . Table 5 shows demonstrates that on average, the model assigns most importance (31.1% relative weight) to the temperature of the molten salt (T). This is followed by electrolysis voltage (V_e) at 26.7%, and active material mass (M) at 23.0%. Finally, duration of electrolysis (D) receives the lowest relative weight (19.1%). This is unsurprising, as this setting did not vary at all across the dataset (see Table 3), so could not explain any of the variance in the predicted output.

A key limitation of the machine learning setup lies in the limited diversity of the input features. Although each of the five cycles contains 264 samples, all samples within a given cycle share the same experimental conditions; the only varying factor is the voltage step. Moreover, the voltage progression itself is identical across all cycles. Thus, even though a unique feature vector exists for each point, the dataset comprises only 5 unique condition vectors across 1320 samples. This extremely low condition variance substantially constrains the expressive capacity available to the model and limits the generalisability of the learned representations. In this context, the fact that the model exhibits meaningful performance at all is somewhat surprising, and underscores the need for more diverse experimental conditions (i.e., a wider range of these conditions) in future studies.

5. Conclusion

This study demonstrates the successful application of electrochemically activated carbon derived from plastic and tyre waste as a sustainable electrode material for supercapacitors. The electrochemical molten salts (EMS) process offers a promising approach for activating black carbon, a waste byproduct from tyre recycling, into high-performance carbon materials suitable for energy storage applications. This study revealed a significant improvement in carbon properties post-EMS activation, as evidenced by a 39.4% increase in BET-estimated surface area (from $43.1 \text{ m}^2 \cdot \text{g}^{-1}$ to $60.09 \text{ m}^2 \cdot \text{g}^{-1}$) and enhanced pore characteristics, including a rise in pore volume and a shift in average pore size. These findings establish the EMS process as an effective and scalable method for producing porous carbon materials, laying the groundwork for optimising black carbon pre-treatment and activation protocols to maximize its electrochemical performance. The use of ethaline, a deep eutectic solvent, as an electrolyte for supercapacitors constructed with EMS-activated carbon demonstrates significant potential when compared to traditional water-based, organic, and other DES electrolytes. The specific capacitance of $110.16 \text{ F} \cdot \text{g}^{-1}$ achieved with ethaline surpasses benchmarks for many conventional aqueous and organic systems, reflecting its superior ionic conductivity and compatibility with activated carbon. The study highlights the importance of further electrochemical testing and characterisation of ethaline and similar DES electrolytes to better understand their behaviour and interaction with EMS activated black carbon, considered a discarded product from recycling tyre waste. Such evaluations could unlock new pathways for developing sustainable supercapacitors and batteries, combining green electrolytes with waste-derived electrode materials to achieve high performance and environmental sustainability.

The study further proposes a useful machine learning framework for the prediction of specific capacitance given black carbon treatment conditions. The framework demonstrates that incorporating physically motivated supervision substantially improves predictive performance. Amongst the evaluated configurations, that which combines dropout, area-based loss, and trainable condition scaling achieves the smallest average deviation from the C_{sp} baseline. While the inclusion of the area-based loss consistently reduced prediction error relative to configurations without it, the smoothness and area losses appear to impose partially competing constraints: combining them slightly increases error compared to using the area loss alone. The lowest error is obtained when the smoothing term is removed and condition scaling is introduced, yielding an average relative error of 3.75%. Analysis of the learned condition weights further provides physically interpretable results: the model assigns the greatest importance to molten salt temperature, followed by electrolysis voltage and active material mass, whereas electrolysis duration contributes least – consistent with its lack of variation across the dataset. Together, these findings indicate that integrating domain-informed loss design with

adaptive condition weighting improves both accuracy and interpretability in predicting specific capacitance

References

- [1] Abdelkader, A.M., Vallés, C., Cooper, A.J., Kinloch, I.A., Dryfe, R.A.W., 2014. Alkali Reduction of Graphene Oxide in Molten Halide Salts: Production of Corrugated Graphene Derivatives for High-Performance Supercapacitors. *ACS Nano* 8, 11225–11233. doi:[10.1021/nm505700x](https://doi.org/10.1021/nm505700x).
- [2] Acevedo, B., Barriocanal, C., Lupul, I., Gryglewicz, G., 2015. Properties and performance of mesoporous activated carbons from scrap tyres, bituminous wastes and coal. *Fuel* 151, 83–90. doi:[10.1016/j.fuel.2015.01.010](https://doi.org/10.1016/j.fuel.2015.01.010).
- [3] Agarap, A.F., 2019. Deep Learning using Rectified Linear Units (ReLU). doi:[10.48550/arXiv.1803.08375](https://doi.org/10.48550/arXiv.1803.08375), arXiv:1803.08375.
- [4] Amir, M., Deshmukh, R.G., Khalid, H.M., Said, Z., Raza, A., Muyeen, S.M., Nizami, A.S., Elavarasan, R.M., Saidur, R., Sopian, K., 2023. Energy storage technologies: An integrated survey of developments, global economical/environmental effects, optimal scheduling model, and sustainable adaption policies. *Journal of Energy Storage* 72, 108694. doi:[10.1016/j.est.2023.108694](https://doi.org/10.1016/j.est.2023.108694).
- [5] Askaruly, K., Korobeinyk, A.V., Azat, S., Yeleuov, M., Taurbekov, A., Toshtay, K., Tuanov, Z., Su, X., 2023. The electrochemical behavior of silica and activated carbon materials derived from the rice husk waste for li-ion cells. *Diamond and Related Materials* 133, 109759. doi:[10.1016/j.diamond.2023.109759](https://doi.org/10.1016/j.diamond.2023.109759).
- [6] Azman, N.H.N., Mamat @ Mat Nazir, M.S., Ngee, L.H., Sulaiman, Y., 2018. Graphene-based ternary composites for supercapacitors. *International Journal of Energy Research* 42, 2104–2116. doi:[10.1002/er.4001](https://doi.org/10.1002/er.4001).
- [7] Banerjee, S., Sinha, P., Verma, K.D., Pal, T., De, B., Cherusseri, J., Manna, P.K., Kar, K.K., 2020. Capacitor to Supercapacitor, in: Kar, K.K. (Ed.), *Handbook of Nanocomposite Supercapacitor Materials I: Characteristics*. Springer International Publishing, Cham, pp. 53–89. doi:[10.1007/978-3-030-43009-2_2](https://doi.org/10.1007/978-3-030-43009-2_2).
- [8] Barlow, A.J., Popescu, S., Artyushkova, K., Scott, O., Sano, N., Hedley, J., Cumpson, P.J., 2016. Chemically specific identification of carbon in XPS imaging using Multivariate Auger Feature Imaging (MAFI). *Carbon* 107, 190–197. doi:[10.1016/j.carbon.2016.05.073](https://doi.org/10.1016/j.carbon.2016.05.073).
- [9] Bridle, J.S., 1989. Training stochastic model recognition algorithms as networks can lead to maximum mutual information estimation of parameters, in: *Proceedings of the 3rd International Conference on Neural Information Processing Systems*, MIT Press, Cambridge, MA, USA. pp. 211–217.
- [10] Burke, G.M., Wurster, D.E., Berg, M.J., Veng-Pedersen, P., Schottelius, D.D., 1992. Surface characterization of activated charcoal by X-ray photoelectron spectroscopy (XPS): Correlation with phenobarbital adsorption data. *Pharmaceutical Research* 9, 126–130. doi:[10.1023/a:1018900431661](https://doi.org/10.1023/a:1018900431661).
- [11] Chen, K., Zhang, T., Chen, X., He, Y., Liang, X., 2018. Model construction of micro-pores in shale: A case study of Silurian Longmaxi Formation shale in Dianqianbei area, SW China. *Petroleum Exploration and Development* 45, 412–421. doi:[10.1016/S1876-3804\(18\)30046-6](https://doi.org/10.1016/S1876-3804(18)30046-6).
- [12] Cheng, R., Xu, J., Wang, X., Ma, Q., Su, H., Yang, W., Xu, Q., 2020. Electrochemical Characteristics and Transport Properties of V(II)/V(III) Redox Couple in a Deep Eutectic Solvent: Magnetic Field Effect. *Frontiers in Chemistry* 8, 549986. doi:[10.3389/fchem.2020.00619](https://doi.org/10.3389/fchem.2020.00619)/BIBTEX.
- [13] Colom, X., Faliq, A., Formela, K., Cañavate, J., 2016. FTIR spectroscopic and thermogravimetric characterization of ground tyre rubber devulcanized by microwave treatment. *Polymer Testing* 52, 200–208. doi:[10.1016/j.polymertesting.2016.04.020](https://doi.org/10.1016/j.polymertesting.2016.04.020).
- [14] Crucean, D., Pontoire, B., Debucquet, G., Le-Bail, A., Le-Bail, P., 2023. The use of choline chloride for salt reduction and texture enhancement in bread. *Applied Food Research* 3, 100371. doi:[10.1016/j.afres.2023.100371](https://doi.org/10.1016/j.afres.2023.100371).
- [15] Dai, L., Karakas, O., Cheng, Y., Cobb, K., Chen, P., Ruan, R., 2023. A review on carbon materials production from plastic wastes. *Chemical Engineering Journal* 453, 139725. doi:[10.1016/j.cej.2022.139725](https://doi.org/10.1016/j.cej.2022.139725).
- [16] De, B., Banerjee, S., Verma, K.D., Pal, T., Manna, P.K., Kar, K.K., 2020. Carbon Nanotube as Electrode Materials for Supercapacitors, in: Kar, K.K. (Ed.), *Handbook of Nanocomposite Supercapacitor Materials II: Performance*. Springer International Publishing, Cham, pp. 229–243. doi:[10.1007/978-3-030-52359-6_9](https://doi.org/10.1007/978-3-030-52359-6_9).
- [17] de Sousa, F.D.B., Scuracchio, C.H., Hu, G.H., Hoppe, S., 2017. Devulcanization of waste tire rubber by microwaves. *Polymer Degradation and Stability* 138, 169–181. doi:[10.1016/j.polymdegradstab.2017.03.008](https://doi.org/10.1016/j.polymdegradstab.2017.03.008).
- [18] Deebansok, S., Deng, J., Le Calvez, E., Zhu, Y., Crosnier, O., Brousse, T., Fontaine, O., 2024. Capacitive tendency concept alongside supervised machine-learning toward classifying electrochemical behavior of battery and pseudocapacitor materials. *Nature Communications* 15, 1133. doi:[10.1038/s41467-024-45394-w](https://doi.org/10.1038/s41467-024-45394-w).
- [19] Demarconnay, L., Raymundo-Piñero, E., Béguin, F., 2010. A symmetric carbon/carbon supercapacitor operating at 1.6 V by using a neutral aqueous solution. *Electrochemistry Communications* 12, 1275–1278. doi:[10.1016/j.elecom.2010.06.036](https://doi.org/10.1016/j.elecom.2010.06.036).
- [20] Devi, M., Rawat, S., Sharma, S., 2021. A comprehensive review of the pyrolysis process: From carbon nanomaterial synthesis to waste treatment. *Oxford Open Materials Science* 1, itab014. doi:[10.1093/oxfmat/itab014](https://doi.org/10.1093/oxfmat/itab014).
- [21] Du, Y., Wang, M., Ye, X., Liu, B., Han, L., Jafri, S.H.M., Liu, W., Zheng, X., Ning, Y., Li, H., 2023. Advances in the Field of Graphene-Based Composites for Energy–Storage Applications. *Crystals* 13, doi:[10.3390/cryst13060912](https://doi.org/10.3390/cryst13060912).
- [22] Egun, I.L., Liu, Z., Zheng, Y., Wang, Z., Song, J., Hou, Y., Lu, J., Wang, Y., Chen, Z., 2024. Turning waste tyres into carbon electrodes for batteries: Exploring conversion methods, material traits, and performance factors. *Carbon Energy* 6, e571. doi:[10.1002/cey.2571](https://doi.org/10.1002/cey.2571).
- [23] El-Maadawy, M.M., Elzoghby, A.A., Masoud, A.M., Eldeeb, A.M., Naggar, A.M.A.E., Taha, M.H., 2024. Retracted Article: Conversion of carbon black recovered from waste tires into activated carbon via chemical/microwave methods for efficient removal of heavy metal ions from wastewater. *RSC Advances* 14, 6324–6338. doi:[10.1039/DRA00172A](https://doi.org/10.1039/DRA00172A).
- [24] Elgrishi, N., Rountree, K.J., McCarthy, B.D., Rountree, E.S., Eisenhart, T.T., Dempsey, J.L., 2018. A Practical Beginner’s Guide to Cyclic Voltammetry. *Journal of Chemical Education* 95, 197–206. doi:[10.1021/acs.jchemed.7b00361](https://doi.org/10.1021/acs.jchemed.7b00361).
- [25] Eren, E.O., Esen, C., Scoppola, E., Song, Z., Senokos, E., Zschiesche, H., Cruz, D., Lauermann, I., Tarakina, N.V., Kumru, B., Antonietti, M., Giusto, P., 2024. Microporous Sulfur–Carbon Materials with Extended Sodium Storage Window. *Advanced Science* 11, 2310196. doi:[10.1002/advs.202310196](https://doi.org/10.1002/advs.202310196).
- [26] Fernando, N., Veldhuizen, H., Nagai, A., Van der Zwaag, S., Abdulkader, A., 2022. Layer-by-layer electrode fabrication for improved performance of porous polyimide-based supercapacitors. *Materials* 15, 4. doi:[10.3390/MA15010004](https://doi.org/10.3390/MA15010004)/S1.
- [27] Fischer, J., Pohle, B., Dmitrieva, E., Thümmler, K., Fischer, S., Mikhailova, D., 2022. Symmetric supercapacitors with cellulose-derived carbons and Na₂SO₄ electrolytes operating in a wide temperature range. *Journal of Energy Storage* 55, 105725. doi:[10.1016/j.est.2022.105725](https://doi.org/10.1016/j.est.2022.105725).
- [28] Frackowiak, E., 2007. Carbon materials for supercapacitor application. *Physical Chemistry Chemical Physics* 9, 1774–1785. doi:[10.1039/B618139M](https://doi.org/10.1039/B618139M).
- [29] Geuchen, P., Jahn, T., Matt, H., 2025. Universal approximation with complex-valued deep narrow neural networks. *Constructive Approximation* 62, 361–402. doi:[10.1007/s00365-025-09713-8](https://doi.org/10.1007/s00365-025-09713-8).
- [30] Ghosh, S., Ryder, K., Roy, S., 2014. Electrochemical and transport properties of ethaline containing copper and tin chloride. *Transactions of the IMF* 92, 41–46. doi:[10.1179/0020296713.000000000133](https://doi.org/10.1179/0020296713.000000000133).
- [31] Girgis, B.S., Temerk, Y.M., Gadelrab, M.M., Abdullah, I.D., 2007. X-ray Diffraction Patterns of Activated Carbons Prepared under Various

- Conditions. *Carbon Letters* 8, 95–100.
- [32] González-González, R.B., González, L.T., Iglesias-González, S., González-González, E., Martínez-Chapa, S.O., Madou, M., Alvarez, M.M., Mendoza, A., 2020. Characterization of Chemically Activated Pyrolytic Carbon Black Derived from Waste Tires as a Candidate for Nanomaterial Precursor. *Nanomaterials* 2020, Vol. 10, Page 2213 10, 2213. doi:10.3390/NANO10112213.
- [33] Gryglewicz, G., Machnikowski, J., Lorenc-Grabowska, E., Lota, G., Frackowiak, E., 2005. Effect of pore size distribution of coal-based activated carbons on double layer capacitance. *Electrochimica Acta* 50, 1197–1206. doi:10.1016/j.electacta.2004.07.045.
- [34] Hemati, S., Hossain, R., Sahajwalla, V., 2021. Selective Thermal Transformation of Automotive Shredder Residues into High-Value Nano Silicon Carbide. *Nanomaterials* 11. doi:10.3390/nano11112781.
- [35] Hou, S., Zhang, D., Xie, Z., Kang, Y., Tang, Z., Dai, Y., Lei, Y., Chen, J., Liang, F., 2022. Activated carbon prepared from waste tire pyrolysis carbon black via CO₂/KOH activation used as supercapacitor electrode. *Science China Technological Sciences* 65, 2337–2347. doi:10.1007/s11431-021-2032-3.
- [36] Hu, Z., Srinivasan, M.P., 1999. Preparation of high-surface-area activated carbons from coconut shell. *Microporous and Mesoporous Materials* 27, 11–18. doi:10.1016/S1387-1811(98)00183-8.
- [37] Inamuddin, Altalhi, T., Adnan, S.M. (Eds.), 2023. Sustainable Materials for Electrochemical Capacitors. 1 ed., Wiley. doi:10.1002/9781394167104.
- [38] Ismail, H.K., Alesary, H.F., Juma, J.A., Hillman, A.R., Ryder, K.S., 2022. A comparative study of the formation, and ion and solvent transport of polyaniline in protic liquid-based deep eutectic solvents and aqueous solutions using EQCM. *Electrochimica Acta* 418, 140348. doi:10.1016/j.electacta.2022.140348.
- [39] Jänes, A., Kurig, H., Lust, E., 2007. Characterisation of activated nanoporous carbon for supercapacitor electrode materials. *Carbon* 45, 1226–1233. doi:10.1016/j.carbon.2007.01.024.
- [40] Jia, Y., Zhou, Z., Chen, D., Li, E., Jiang, Z., Zhao, L., Guo, L., 2024. Recent advances in molten salt CO₂ capture and electrochemical conversion to functional carbon materials. *Journal of Industrial and Engineering Chemistry* 134, 17–27. doi:10.1016/J.JIEC.2023.12.054.
- [41] Jiang, G., Guo, J., Sun, Y., Liu, X., Pan, J., 2021. Pyrolytic carbon black-derived porous carbon with spherical skeleton as recovered and enduring electrode material for supercapacitor. *Journal of Energy Storage* 44, 103372. doi:10.1016/j.est.2021.103372.
- [42] Jiang, H., Shao, J., Hu, Q., Zhu, Y., Cheng, W., Zhang, J., Fan, T., Yu, J., Yang, H., Zhang, X., Chen, H., 2024. Carbon black production characteristics and mechanisms from pyrolysis of rubbers. *Fuel Processing Technology* 253, 108011. doi:10.1016/j.fuproc.2023.108011.
- [43] Jiang, L., Zhao, L., Chen, G., Li, M., Zhang, R., 2022. Graphite-enhanced thermal properties of octadecylamine/graphite foam shape-stable composite phase change materials for thermal energy storage. *Energy Reports* 8, 13939–13947. doi:10.1016/j.egyr.2022.10.121.
- [44] Jovičić, M., Bera, O., Stojanov, S., Pavličević, J., Govđedarica, D., Bobinac, I., Hollo, B.B., 2023. Effects of recycled carbon black generated from waste rubber on the curing process and properties of new natural rubber composites. *Polymer Bulletin* 80, 5047–5069. doi:10.1007/s00289-022-04307-x.
- [45] Kalkan, E., Arvas, M.B., Yazar, S., Sahin, Y., 2023. Investigation of supercapacitor electrode performances of phosphorus-doped graphene oxide electrodes in various deep eutectic solvents and symmetric supercapacitor application. *Journal of Energy Storage* 73, 109184. doi:10.1016/j.est.2023.109184.
- [46] Kamali, A.R., 2020. Green production of carbon nanomaterials in molten salts and applications. *Green Production of Carbon Nanomaterials in Molten Salts and Applications*, 1–162doi:10.1007/978-981-15-2373-1/COVER.
- [47] Kamali, A.R., Fray, D.J., 2014. Towards large scale preparation of carbon nanostructures in molten LiCl. *Carbon* 77, 835–845. doi:10.1016/J.CARBON.2014.05.089.
- [48] Kan, Y., Ning, G., Ma, X., 2017. Sulfur-decorated nanomesh graphene for high-performance supercapacitors. *Chinese Chemical Letters* 28, 2277–2280. doi:10.1016/j.ccl.2017.11.026.
- [49] Kar, T., Shetty, V.R., Pasha, S.K., Deshmukh, K., Godavarthi, S., Kesarla, M.K., 2023. Development of symmetric and asymmetric supercapacitors—a step towards efficient and practical energy storage, in: *Smart Supercapacitors*. Elsevier, pp. 405–456. doi:10.1016/B978-0-323-90530-5.00013-7.
- [50] Karnan, M., Raj, A.G., Subramani, K., Santhoshkumar, S., Sathish, M., 2020. The fascinating supercapacitive performance of activated carbon electrodes with enhanced energy density in multifarious electrolytes. *Sustainable Energy & Fuels* 4, 3029–3041. doi:10.1039/C9SE01298B.
- [51] Kasprzak, D., Galiński, M., 2022. Biopolymer-based gel electrolytes with an ionic liquid for high-voltage electrochemical capacitors. *Electrochemistry Communications* 138, 107282. doi:10.1016/j.elcom.2022.107282.
- [52] Keppetipola, N.M., Dissanayake, M., Dissanayake, P., Karunaratne, B., Dourges, M.A., Talaga, D., Servant, L., Olivier, C., Toupane, T., Uchida, S., Tennakone, K., Kumara, G.R.A., Cojocaru, L., 2021. Graphite-type activated carbon from coconut shell: A natural source for eco-friendly non-volatile storage devices. *RSC Advances* 11, 2854–2865. doi:10.1039/D0RA09182K.
- [53] Khosrozadeh, A., Tao, L., Zhao, P., Miller, M.B., Voznyy, O., Liu, J., 2021. Water/acetonitrile hybrid electrolyte enables using smaller ions for achieving superior energy density in carbon-based supercapacitors. *Journal of Power Sources* 498, 229905. doi:10.1016/j.jpowsour.2021.229905.
- [54] Kim, Y.S., Kim, M.K., Fu, N., Liu, J., Wang, J., Srebric, J., 2025. Investigating the impact of data normalization methods on predicting electricity consumption in a building using different artificial neural network models. *Sustainable Cities and Society* 118, 105570. doi:10.1016/j.scs.2024.105570.
- [55] Kumar Yogesh, G., Nandi, D., Yeetsorn, R., Wanchan, W., Devi, C., Pratap Singh, R., Vasistha, A., Kumar, M., Koinkar, P., Yadav, K., 2025. A machine learning approach for estimating supercapacitor performance of graphene oxide nano-ring based electrode materials. *Energy Advances* 4, 119–139. doi:10.1039/D4YA00577E.
- [56] Kusi, D.A., Arthur, E.K., Gikunu, E., Dzikunu, P., Asiedu, K.K., Armoo, R., Agyemang, F.O., 2024. Electrochemical performance of chemically treated pyrolytic carbon black from waste car tyres. *Energy Nexus* 14, 100297. doi:10.1016/j.nexus.2024.100297.
- [57] Lazanas, A.C., Prodromidis, M.I., 2023. Electrochemical Impedance Spectroscopy-A Tutorial. *ACS measurement science au* 3, 162–193. doi:10.1021/acsmmeasuresciau.2c00070.
- [58] Li, H., Bucci, G., Brady, N.W., Cross, N.R., Ehlinger, V.M., Lin, T.Y., Salazar De Troya, M., Tortorelli, D., Worsley, M.A., Roy, T., 2024. Topology optimization for the full-cell design of porous electrodes in electrochemical energy storage devices. *Structural and Multidisciplinary Optimization* 67, 188. doi:10.1007/s00158-024-03901-z.
- [59] Liu, T., Zhang, L., Cheng, B., Hu, X., Yu, J., 2020. Holey Graphene for Electrochemical Energy Storage. *Cell Reports Physical Science* 1, 100215. doi:10.1016/j.xrpp.2020.100215.
- [60] Liu, X., Fechner, N., Antonietti, M., 2013. Salt melt synthesis of ceramics, semiconductors and carbon nanostructures. *Chemical Society Reviews* 42, 8237–8265. doi:10.1039/C3CS60159E.
- [61] Long, C.M., Nasarella, M.A., Valberg, P.A., 2013. Carbon black vs. black carbon and other airborne materials containing elemental carbon: Physical and chemical distinctions. *Environmental Pollution* 181, 271–286. doi:10.1016/J.ENVPOL.2013.06.009.
- [62] Miao, L., Song, Z., Zhu, D., Li, L., Gan, L., Liu, M., 2020. Recent advances in carbon-based supercapacitors. *Materials Advances* 1, 945–966. doi:10.1039/D0MA00384K.
- [63] Mishra, B., Olson, D.L., 2005. Molten salt applications in materials processing. *Journal of Physics and Chemistry of Solids* 66, 396–401. doi:10.1016/j.jpcs.2004.06.049.
- [64] Mishra, Y., Chattaraj, A., Aljabali, A.A., El-Tanani, M., Tambuwala, M.M., Mishra, V., 2024. Graphene oxide-lithium-ion batteries:

- Inauguration of an era in energy storage technology. *Clean Energy* 8, 194–205. doi:[10.1093/ce/zkd095](https://doi.org/10.1093/ce/zkd095).
- [65] Mou, W., Zhou, Y., Gao, J., Wang, L., 2018. Dropout Training, Data-dependent Regularization, and Generalization Bounds, in: Proceedings of the 35th International Conference on Machine Learning, PMLR. pp. 3645–3653.
- [66] Muñoz, P.M., Humana, R.M., Falaguerra, T., Correa, G., 2020. Parameter optimization of an electrochemical and thermal model for a lithium-ion commercial battery. *Journal of Energy Storage* 32, 101803. doi:[10.1016/j.est.2020.101803](https://doi.org/10.1016/j.est.2020.101803).
- [67] Mursal, N., Shelake, A.R., Ahir, S.A., Sonawane, P.P., Selvaraj, M., Assiri, M.A., Kulkarni, S.V., Sutar, S.S., Amate, R.U., Jeon, C.W., Dongale, T.D., Shah, P.P., 2025. From data to device: Machine learning-driven optimization, predictions, and experimental insights for engineering high-performance MnO₂ supercapacitors. *Colloids and Surfaces A: Physicochemical and Engineering Aspects* 727, 138392. doi:[10.1016/j.colsurfa.2025.138392](https://doi.org/10.1016/j.colsurfa.2025.138392).
- [68] Navalpotro, P., Anderson, M., Marcilla, R., Palma, J., 2018. Insights into the energy storage mechanism of hybrid supercapacitors with redox electrolytes by Electrochemical Impedance Spectroscopy. *Electrochimica Acta* 263, 110–117. doi:[10.1016/j.electacta.2017.12.167](https://doi.org/10.1016/j.electacta.2017.12.167).
- [69] Navarro-Suárez, A., Johansson, P., 2020. Perspective—Semi-Solid Electrolytes Based on Deep Eutectic Solvents: Opportunities and Future Directions. *Journal of The Electrochemical Society* 167, 070511. doi:[10.1149/1945-7111/ab68d3](https://doi.org/10.1149/1945-7111/ab68d3).
- [70] Neethirajan, J., Parathodika, A.R., Hu, G.H., Naskar, K., 2022. Functional rubber composites based on silica-silane reinforcement for green tire application: The state of the art. *Functional Composite Materials* 3, 7. doi:[10.1186/s42252-022-00035-7](https://doi.org/10.1186/s42252-022-00035-7).
- [71] Nguyen, T.D.H., Lin, S.Y., Chung, H.C., Tran, N.T.T., Lin, M.F. (Eds.), 2021. First-Principles Calculations for Cathode, Electrolyte and Anode Battery Materials. IOP Publishing. doi:[10.1088/978-0-7503-4685-6](https://doi.org/10.1088/978-0-7503-4685-6).
- [72] Pan, H., Li, J., Feng, Y., 2010. Carbon Nanotubes for Supercapacitor. *Nanoscale Research Letters* 5, 654. doi:[10.1007/s11671-009-9508-2](https://doi.org/10.1007/s11671-009-9508-2).
- [73] Pettersson, F., Keskinen, J., Remonen, T., von Herten, L., Jansson, E., Tappura, K., Zhang, Y., Wilén, C.E., Österbacka, R., 2014. Printed environmentally friendly supercapacitors with ionic liquid electrolytes on paper. *Journal of Power Sources* 271, 298–304. doi:[10.1016/j.jpowsour.2014.08.020](https://doi.org/10.1016/j.jpowsour.2014.08.020).
- [74] Poonam, Sharma, K., Arora, A., Tripathi, S.K., 2019. Review of supercapacitors: Materials and devices. *Journal of Energy Storage* 21, 801–825. doi:[10.1016/j.est.2019.01.010](https://doi.org/10.1016/j.est.2019.01.010).
- [75] Rajarao, R., Farzana, R., Khanna, R., Sahajwalla, V., 2015. Synthesis of SiC/Si₃N₄ nanocomposite by using automotive waste tyres as resource. *Journal of Industrial and Engineering Chemistry* 29, 35–38. doi:[10.1016/j.jiec.2015.04.006](https://doi.org/10.1016/j.jiec.2015.04.006).
- [76] Ravichandran, A., Raman, V., Selvaraj, Y., Mohanraj, P., Kuzhandaivel, H., 2024. Machine Learning-Based Prediction of Cyclic Voltammetry Behavior of Substitution of Zinc and Cobalt in BiFeO₃/Bi₂FeO₄ for Supercapacitor Applications. *ACS Omega* 9, 33459–33470. doi:[10.1021/acsomega.3c10485](https://doi.org/10.1021/acsomega.3c10485).
- [77] Reza Kamali, A., J. Fray, D., 2015. Large-scale preparation of graphene by high temperature insertion of hydrogen into graphite. *Nanoscale* 7, 11310–11320. doi:[10.1039/C5NR01132A](https://doi.org/10.1039/C5NR01132A).
- [78] Rodriguez-Loya, J., Lerma, M., Gardea-Torresdey, J.L., 2023. Dynamic Light Scattering and Its Application to Control Nanoparticle Aggregation in Colloidal Systems: A Review. *Micromachines* 15. doi:[10.3390/mi15010024](https://doi.org/10.3390/mi15010024).
- [79] Roetman, E., Joustra, J., Heideman, G., Balkenende, R., 2024. Does the Rubber Meet the Road? Assessing the Potential of Devulcanization Technologies for the Innovation of Tire Rubber Recycling. *Sustainability* 16. doi:[10.3390/su16072900](https://doi.org/10.3390/su16072900).
- [80] Roman, D., Saxena, S., Bruns, J., Valentin, R., Pecht, M., Flynn, D., 2021. A Machine Learning Degradation Model for Electrochemical Capacitors Operated at High Temperature doi:[10.1109/ACCESS.2021.3057959](https://doi.org/10.1109/ACCESS.2021.3057959).
- [81] Sathiskumar, C., Karthikeyan, S., 2019. Recycling of waste tires and its energy storage application of by-products –a review. *Sustainable Materials and Technologies* 22, e00125. doi:[10.1016/j.susmat.2019.00125](https://doi.org/10.1016/j.susmat.2019.00125).
- [82] Sazali, A.L., AlMasoud, N., Amran, S.K., Alomar, T.S., Pa'ee, K.F., El-Bahy, Z.M., Yong, T.L.K., Dailin, D.J., Chuah, L.F., 2023. Physicochemical and thermal characteristics of choline chloride-based deep eutectic solvents. *Chemosphere* 338, 139485. doi:[10.1016/j.chemosphere.2023.139485](https://doi.org/10.1016/j.chemosphere.2023.139485).
- [83] Schmidt, J., Marques, M.R.G., Botti, S., Marques, M.A.L., . Recent advances and applications of machine learning in solid-state materials science doi:[10.1038/s41524-019-0221-0](https://doi.org/10.1038/s41524-019-0221-0).
- [84] Schneider, D., Mehlhorn, D., Zeigermann, P., Kärger, J., Valiullin, R., 2016. Transport properties of hierarchical micro-mesoporous materials. *Chemical Society Reviews* 45, 3439–3467. doi:[10.1039/C5CS00715A](https://doi.org/10.1039/C5CS00715A).
- [85] Schuepfer, D.B., Badaczewski, F., Guerra-Castro, J.M., Hofmann, D.M., Heiliger, C., Smarsly, B., Klar, P.J., 2020. Assessing the structural properties of graphitic and non-graphitic carbons by Raman spectroscopy. *Carbon* 161, 359–372. doi:[10.1016/j.carbon.2019.12.094](https://doi.org/10.1016/j.carbon.2019.12.094).
- [86] Shaheen Shah, S., Abu Nayem, S.M., Sultana, N., Saleh Ahammad, A.J., Abdul Aziz, M., 2022. Preparation of Sulfur-doped Carbon for Supercapacitor Applications: A Review. *ChemSusChem* 15, e202101282. doi:[10.1002/cssc.202101282](https://doi.org/10.1002/cssc.202101282).
- [87] Sharma, A., Sawant, R.J., Sharma, A., Joshi, J.B., Jain, R.K., Kasilingam, R., 2022. Valorisation of End-of-Life tyres for generating valuable resources under circular economy. *Fuel* 314, 123138. doi:[10.1016/j.fuel.2022.123138](https://doi.org/10.1016/j.fuel.2022.123138).
- [88] Sharma, P., Kumar, V., 2020. Study of electrode and electrolyte material of supercapacitor. *Materials Today: Proceedings* 33, 1573–1578. doi:[10.1016/j.matpr.2020.04.694](https://doi.org/10.1016/j.matpr.2020.04.694).
- [89] Sharma, S., Chand, P., 2023. Supercapacitor and electrochemical techniques: A brief review. *Results in Chemistry* 5, 100885. doi:[10.1016/j.rechem.2023.100885](https://doi.org/10.1016/j.rechem.2023.100885).
- [90] Shelake, A.R., Karade, V.C., Selvaraj, M., Assiri, M.A., More, D.D., Patil, A.D., Mali, M.G., Sutar, S.S., Amate, R.U., Jeon, C.W., Kim, T.G., Dongale, T.D., 2026. Machine learning-guided optimization, predictive modeling, and experimental validation of MXene-based supercapacitors. *Journal of Power Sources* 663, 238863. doi:[10.1016/j.jpowsour.2025.238863](https://doi.org/10.1016/j.jpowsour.2025.238863).
- [91] Sinclair, N., Shen, X., Wainright, J.S., 2021. Electrochemical Decomposition of Ethylene Glycol-Choline Chloride Deep Eutectic Solvent. *ECS Meeting Abstracts MA2021-01*, 25. doi:[10.1149/MA2021-01125mtgabs](https://doi.org/10.1149/MA2021-01125mtgabs).
- [92] Singh, P., Sharma, R.K., Khalid, M., Goyal, R., Sari, A., Tyagi, V.V., 2022. Evaluation of carbon based-supporting materials for developing form-stable organic phase change materials for thermal energy storage: A review. *Solar Energy Materials and Solar Cells* 246, 111896. doi:[10.1016/j.solmat.2022.111896](https://doi.org/10.1016/j.solmat.2022.111896).
- [93] Smith, E.L., Abbott, A.P., Ryder, K.S., 2014. Deep Eutectic Solvents (DESs) and Their Applications. *Chemical Reviews* 114, 11060–11082. doi:[10.1021/cr300162p](https://doi.org/10.1021/cr300162p).
- [94] Srivastava, N., Hinton, G., Krizhevsky, A., Sutskever, I., Salakhutdinov, R., 2014. Dropout: A Simple Way to Prevent Neural Networks from Overfitting. *Journal of Machine Learning Research* 15, 1929–1958.
- [95] Sugatri, R.I., Wirasadewa, Y.C., Saputro, K.E., Muslih, E.Y., Ikono, R., Nasir, M., 2018. Recycled carbon black from waste of tire industry: Thermal study. *Microsystem Technologies* 24, 749–755. doi:[10.1007/s00542-017-3397-6](https://doi.org/10.1007/s00542-017-3397-6).
- [96] Sun, M.H., Huang, S.Z., Chen, L.H., Li, Y., Yang, X.Y., Yuan, Z.Y., Su, B.L., 2016. Applications of hierarchically structured porous materials from energy storage and conversion, catalysis, photocatalysis, adsorption, separation, and sensing to biomedicine. *Chemical Society Reviews* 45, 3479–3563. doi:[10.1039/C6CS00135A](https://doi.org/10.1039/C6CS00135A).

- [97] Tajik, M., Makui, A., Tosarkani, B.M., 2023. Sustainable cathode material selection in lithium-ion batteries using a novel hybrid multi-criteria decision-making. *Journal of Energy Storage* 66, 107089. doi:[10.1016/j.est.2023.107089](https://doi.org/10.1016/j.est.2023.107089).
- [98] Takagi, H., Maruyama, K., Yoshizawa, N., Yamada, Y., Sato, Y., 2004. XRD analysis of carbon stacking structure in coal during heat treatment. *Fuel* 83, 2427–2433. doi:[10.1016/j.fuel.2004.06.019](https://doi.org/10.1016/j.fuel.2004.06.019).
- [99] Thillaikkarasi, D., Karthikeyan, S., Ramesh, R., Sengodan, P., Kavitha, D., Muthubalasubramanian, M., 2022. Electrochemical performance of various activated carbon-multi-walled carbon nanotubes symmetric supercapacitor electrodes in aqueous electrolytes. *Carbon Letters* 32, 1481–1505. doi:[10.1007/s42823-022-00386-y](https://doi.org/10.1007/s42823-022-00386-y).
- [100] Thomas, P., Lai, C.W., Bin Johan, M.R., 2019. Recent developments in biomass-derived carbon as a potential sustainable material for super-capacitor-based energy storage and environmental applications. *Journal of Analytical and Applied Pyrolysis* 140, 54–85. doi:[10.1016/j.jaap.2019.03.021](https://doi.org/10.1016/j.jaap.2019.03.021).
- [101] Ungár, T., Gubicza, J., Ribárik, G., Pantea, C., Zerda, T.W., 2002. Microstructure of carbon blacks determined by X-ray diffraction profile analysis. *Carbon* 40, 929–937. doi:[10.1016/S0008-6223\(01\)00224-X](https://doi.org/10.1016/S0008-6223(01)00224-X).
- [102] Verma, S., Das, T., Verma, S., Pandey, V.K., Pandey, S.K., Singh, J., Verma, B., 2026. Carbon Nanotube as Electrode Material for Supercapacitors, in: *Handbook of Energy Materials in Supercapacitors and Storage Devices*. John Wiley & Sons, Ltd. chapter 7, pp. 161–173. doi:[10.1002/9781119901259.ch7](https://doi.org/10.1002/9781119901259.ch7).
- [103] Wang, C., Huang, J., Li, J., Cao, L., Kajiyoshi, K., 2022. Two C-S bonds derived from carbons with different IG>ID values promote high sulfur loads and stable capacity storage. *Applied Surface Science* 584, 152620. doi:[10.1016/j.apsusc.2022.152620](https://doi.org/10.1016/j.apsusc.2022.152620).
- [104] Watanabe, M., Thomas, M.L., Zhang, S., Ueno, K., Yasuda, T., Dokko, K., 2017. Application of Ionic Liquids to Energy Storage and Conversion Materials and Devices. *Chemical Reviews* 117, 7190–7239. doi:[10.1021/ACS.CHEMREV.6B00504/ASSET/IMAGES/LARGE/CR-2016-00504M_0037.JPG](https://doi.org/10.1021/ACS.CHEMREV.6B00504/ASSET/IMAGES/LARGE/CR-2016-00504M_0037.JPG).
- [105] Wu, L., Li, Y., Fu, Z., Su, B.L., 2020. Hierarchically structured porous materials: Synthesis strategies and applications in energy storage. *National Science Review* 7, 1667–1701. doi:[10.1093/nsr/nwaa183](https://doi.org/10.1093/nsr/nwaa183).
- [106] Xie, K., Kamali, A.R., 2022. Electrochemical production of hydrogen in molten salt. *Energy Conversion and Management* 251, 114980. doi:[10.1016/j.enconman.2021.114980](https://doi.org/10.1016/j.enconman.2021.114980).
- [107] Xu, L.H., Wu, D., Zhu, Y.W., Chen, X.Y., Zhang, Z.J., 2022. Deep eutectic solvents as effective electrolyte from potassium iodide and ethylene glycol exhibiting redox behavior for supercapacitor application. *Journal of Energy Storage* 48, 103955. doi:[10.1016/j.est.2022.103955](https://doi.org/10.1016/j.est.2022.103955).
- [108] Yang, L., Huang, T., Jiang, X., Jiang, W., 2016. Effect of steam and CO₂ activation on characteristics and desulfurization performance of pyrolusite modified activated carbon. *Adsorption-journal of The International Adsorption Society* 22, 1099–1107. doi:[10.1007/s10450-016-9832-7](https://doi.org/10.1007/s10450-016-9832-7).
- [109] Yu, Z., Wang, X., Hou, Y.N., Pan, X., Zhao, Z., Qiu, J., 2017. Nitrogen-doped mesoporous carbon nanosheets derived from metal-organic frameworks in a molten salt medium for efficient desulfurization. *Carbon* 117, 376–382. doi:[10.1016/j.carbon.2017.02.100](https://doi.org/10.1016/j.carbon.2017.02.100).
- [110] Zhang, Q., Vigier, K.D.O., Royer, S., Jérôme, F., 2012. Deep eutectic solvents: Syntheses, properties and applications. *Chemical Society Reviews* 41, 7108–7146. doi:[10.1039/C2CS35178A](https://doi.org/10.1039/C2CS35178A).
- [111] Zhang, W., Hu, C., Li, J., Zhao, R., Pang, S., Liang, B., Tang, S., 2023. Insight into the origin of oxidation behaviors of carbon fiber reinforced carbon aerogel composites with different porous skeletons. *Carbon* 209, 118008. doi:[10.1016/j.carbon.2023.118008](https://doi.org/10.1016/j.carbon.2023.118008).
- [112] Zhao, L., Li, Y., Yu, M., Peng, Y., Ran, F., 2023. Electrolyte-Wettability Issues and Challenges of Electrode Materials in Electrochemical Energy Storage, Energy Conversion, and Beyond. *Advanced Science* 10, e2300283. doi:[10.1002/advs.202300283](https://doi.org/10.1002/advs.202300283).
- [113] Zheng, S., Han, P., Han, Z., Zhang, H., Tang, Z., Yang, J., 2014. High Performance C/S Composite Cathodes with Conventional Carbonate-Based Electrolytes in Li-S Battery. *Scientific Reports* 4, 4842. doi:[10.1038/srep04842](https://doi.org/10.1038/srep04842).
- [114] Zhu, F., Ge, J., Gao, Y., Li, S., Chen, Y., Tu, J., Wang, M., Jiao, S., 2023. Molten salt electro-preparation of graphitic carbons. *Exploration* 3, 20210186. doi:[10.1002/EXP.20210186](https://doi.org/10.1002/EXP.20210186).
- [115] Zoromba, M.S., Abdel-Aziz, M.H., Bassyouni, M., Gutub, S., Demko, D., Abdelkader, A., 2017. Electrochemical Activation of Graphene at Low Temperature: The Synthesis of Three-Dimensional Nanoarchitectures for High Performance Supercapacitors and Capacitive Deionization. *ACS Sustainable Chemistry & Engineering* 5, 4573–4581. doi:[10.1021/acssuschemeng.6b02869](https://doi.org/10.1021/acssuschemeng.6b02869).